Accepted manuscript of the published article: Miner Petrol (2016) 110:747–765 [DOI 10.1007/s00710-016-0442-6]

Multi-stage evolution of xenotime–(Y) from Písek pegmatites, Czech Republic: An electron probe micro-analysis and Raman spectroscopy study

E. Švecová[1] • R. Čopjaková[1] • Z. Losos[1] • R. Škoda[1] • L. Nasdala[2] • J. Cícha[3]

✉ Z. Losos
losos@sci.muni.cz

[1] Department of Geological Sciences, Faculty of Science, Masaryk University, Kotlářská 2, 611 37 Brno, Czech Republic

[2] Institut für Mineralogie und Kristallographie, Universität Wien, Althanstr. 14, A–1090 Wien, Austria

[3] Prácheň Museum, Velké nám. 114, 397 24 Písek, Czech Republic

Abstract The chemical variability, degree of radiation damage, and alteration of xenotime from the Písek granitic pegmatites (Czech Republic) were investigated by micro-chemical analysis and Raman spectroscopy. Dominant large xenotime–(Y) grains enriched in U, Th and Zr crystallized from a melt almost simultaneously with zircon, monazite and tourmaline. Xenotime is well to poorly crystalline depending on its U and Th contents. It shows complex secondary textures cutting magmatic growth zones as a result of its interaction with F,Ca,alkali-rich fluids during the hydrothermal stage of the pegmatite evolution. The magmatic xenotime underwent intense secondary alteration, from rims inwards, resulting in the formation of inclusion-rich well crystalline xenotime domains of near end-member composition. Two types of recrystallization were distinguished in relation to the type of inclusions: i) xenotime with coffinite-thorite, cheralite and monazite inclusions and ii) xenotime with zirconcheralite and zircon inclusions. Additionally, inner poorly crystalline U,Th-rich xenotime domains were locally altered, hydrated, depleted in P, Y, HREE, U, Si and radiogenic Pb, and enriched in fluid-borne cations (mainly Ca, F, Th, Zr, Fe). Interaction of radiation-damaged xenotime with hydrothermal fluids resulted in the disturbance of the U–Th–Pb system. Alteration of radiation-damaged xenotime was followed by intensive recrystallization indicating the presence of fluids >200 °C. Subsequently other types of xenotime formed as a consequence of fluid-driven alteration of magmatic monazite, and Y,REE,Ti,Nb-oxides or crystallized from hydrothermal fluids along cracks in magmatic monazite and xenotime.

Key words: xenotime-(Y); aqueous fluids; metamictization; recrystallization; alteration; EPMA; Raman spectroscopy

Introduction

Xenotime-(Y), YPO_4, is a tetragonal mineral isostructural with zircon, $ZrSiO_4$. Besides Y, other rare earth elements (REE), predominantly heavy rare earth elements (HREE), and the actinide elements U and Th, are incorporated preferentially at the eight-fold lattice site in the xenotime-(Y) structure (Ni et al. 1995, Vernilli et al. 2007). High actinide concentrations are usually observed in xenotime-(Y) from granitic rocks and their pegmatites (Demartin et al. 1991; Bea 1996; Broska et al. 2005; Hetherington and Harlov 2008). Moreover, xenotime-(Y) typically contains traces of Ca, Si, Zr as well as Sc (e.g. Demartin et al. 1991; Bernhard et al. 1998; Hetherington and Harlov 2008).

Xenotime occurs as a common accessory phase in igneous rocks, where it can bear a significant portion of the whole rock Y+HREE budget (Bea 1996). Primary magmatic xenotime is typical of peraluminous leucogranites and granitic pegmatites (Demartin et al. 1991; Buck et al. 1999; Broska et al. 2005; Hetherington and Harlov 2008). Secondary post-magmatic xenotime can form during late-stage activity of hydrothermal fluids in granites or pegmatites during the cooling of its host rock (Åmli 1975; Hetherington and Harlov 2008; Harlov 2011).

The importance of xenotime in petrology, mainly in geochronology (e.g. Hetherington et al. 2008) and for temperature estimates (e.g. Gratz and Heinrich 1997), has been well documented. Stimulated by the ability of xenotime-group minerals to incorporate notable amounts of actinides, these minerals were studied with regard to their possible use as host ceramics for the long-term storage of radiogenic waste (Ewing 2007; Ewing and Weber 2010). The radiation-induced structural damage of U- and Th-bearing xenotime-(Y) and related minerals has been investigated by various authors (e.g. Pabst 1952; Ewing 1976; Ewing 1994; Tomašić et al. 2008, Talla et al. 2011). However, investigations addressing the hydrothermal alteration of xenotime and related remobilization of U, Th, and Y+REE are rather rare (Broska et al. 2005; Hetherington and Harlov 2008, Hetherington et al. 2010). Studies focusing on the formation of xenotime, and its alteration behavior, are crucial for direct interpretations of geochronological data, understanding of processes that involve remobilization of U, Th, and Y+REE during mineral-fluid interaction and provide valuable information for radioactive waste management.

This present paper documents the results of a comprehensive study of the mineral assemblage and chemical composition of altered and unaltered domains in primary magmatic xenotime-(Y), subsequently recrystallized to altered xenotime-(Y) from three granitic pegmatites of the Písek pegmatite field, Czech Republic. The chemical variability, degree of radiation damage, and alteration of xenotime in relation to its textural characteristics, paragenesis and total cumulative dose, have been investigated by micro-chemical analysis and Raman spectroscopy.

Geological setting

Moldanubian Zone

The Písek pegmatite field is located 5-10 km E from the city of Písek and belongs to the Moldanubian Zone (Fig. 1). The Moldanubian Zone is built up of Precambrian and Paleozoic medium- to high-grade metamorphic rocks (amphibolite to granulite facies) intruded by numerous granitoids and consists of two different tectonometamorphic units: Gföhl and Drosendorf Units

(Franke 2000). The Gföhl Unit represents the structurally highest level of the Moldanubian Zone and includes mainly anatectic orthogneisses, migmatites, granulites, and minor paragneisses, amphibolites, eclogites, peridotites and pyroxenites (e.g. Franke 2000; Janoušek et al. 2004; Medaris et al. 2005; Kotková 2007). The Drosendorf nappe is formed by the Monotonous and the Varied Units. The Monotonous Unit is composed mainly of migmatitic cordierite-biotite-sillimanite paragneisses associated with felsic orthogneisses and minor amphibolites. The Varied Unit contains intercalations of marbles, calc-silicate rocks, amphibolites, quartzites and graphitic gneisses (e.g. Franke 2000; Medaris et al. 1995; Janoušek et al. 2008).

Several important stages of Variscan magmatic activity were distinguished in the Moldanubian Zone (Timmerman 2008): (i) subduction-related calc-alkaline suites (~ 370-345 Ma), (ii) (ultra-)potassic, Mg-rich quartz syenitic to melagranitic plutons; divided into amphibole-biotite melagranite to quartz syenite (durbachite suite; ~ 345-338 Ma), and biotite-two-pyroxene quartz syenites to melagranites (syenitoid suite; ~ 337-335 Ma; Holub 1997; Janoušek and Holub 2007; Žák et al. 2014), and (iii) peraluminous anatectic granites formed as a consequence of the low-pressure/ high-temperature metamorphic overprint (331-326 Ma).

Pegmatites of the Písek pegmatite field

Beryl-bearing pegmatites with abundant tourmaline are characteristic for the Písek pegmatite field. They intruded the migmatized gneisses of the Gföhl Unit and the amphibole-biotite syenites (Fig. 1b; Novák et al. 1998; Novák and Cícha 2009). Novák et al. (1998) have determined a U–Pb age of 339±3 Ma for magmatic monazite from the U Obrázku pegmatite. Pegmatite bodies form lenses and dikes with thicknesses up to 30 m. Zonal internal structure of pegmatites comprises from the rim inwards: a granitic zone (K-feldspar, quartz, plagioclase, biotite), a graphic zone (K-feldspar, quartz, biotite or tourmaline), blocky K-feldspar zone and quartz core (Cícha et al. 2005; Škoda et al. 2011). An albite unit (albite, quartz, ± tourmaline and muscovite), which contains most of accessory minerals, is developed between the quartz core and blocky K-feldspar in more evolved pegmatite dikes (Škoda et al. 2011).

Besides the major constituents quartz, K-feldspar and albite, the pegmatites consist of biotite>muscovite and tourmaline (schorl-dravite and rarely foitite). Accessory minerals include beryl, almandine, cordierite-sekaninaite, fluorapatite, Nb-rich rutile, monazite-(Ce), xenotime-(Y), zircon, Y,REE,Ti,Nb-oxides of the samarskite and polycrase groups (formerly called písekite), columbite, ilmenite, danalite, helvine, arsenopyrite, pyrite, chalcopyrite and molybdenite (Bouška and Johan 1972; Cícha et al. 2005; Novák and Cícha 2009; Škoda et al. 2011). The Y,REE,Ti,Nb-oxides are commonly heavily altered to a mixture of amorphous and hydrated Nb,Ti,U,Y,As,Si,P,Fe,Ca-phase, anatase, columbite-(Fe), ixiolite, rutile, scheelite, pyrochlore-group minerals, torbernite and kahlerite (Škoda et al. 2011). Pharmacosiderite, symplesite, scorodite, delwauxite, pitticite, jarosite and goethite can be found as weathering products of arsenopyrite and pyrite (Novák and Cícha 2009).

Samples and analytical methods

A suite of 24 samples comprising Y+REE-bearing phosphates (xenotime, monazite) from three localities in the Písek pegmatite field havs been investigated (Fig. 1b). Mineral assemblages containing Y+REE-phosphates were separated and embedded in epoxy to produce surface-polished mounts. For electron probe micro-analyser (EPMA) study, the mounts were coated with carbon.

The internal textures and chemical compositions of xenotime and associated phases were investigated by a combination of back-scattered electrons (BSE) images, EPMA data and X-ray element mapping using a CAMECA SX100 system operated in wavelength-dispersion mode . Operating analytical conditions were as follows: accelerating voltage 15 kV, beam current 20–60 nA, and beam diameter 5 μm. Peak-counting times varied from 20 to 180 s in order to optimize the detection limits. The following synthetic and natural calibrant materials were used: U – U metal; Pb - PbSe; Ca, Th - $CaTh(PO_4)_2$; P - $LaPO_4$; Y - YAG; La-Yb - individual $REEPO_4$; Lu - LuAG; Al, Si - sanidine; Fe - andradite; Mn - rhodonite; W - scheelite; As - lammerite; Nb - columbite; Ta - $CrTa_2O_6$; Ti - titanite; Zr - zircon; Sc - $ScVO_4$; S - $BaSO_4$; Sr - $SrSO_4$ and F - topaz. Possible peak overlaps were checked for in detail, and background positions were chosen carefully, by thorough wavelength-dispersive angle scans on natural and synthetic REE-phases. Uranium was determined on the U M_β line (counting time 100 s), Th on the Th M_α line (counting time 60 s) and Pb on the M_α line (counting time 180 s). More details concerning analytical conditions for REE-bearing and Zr-Th-U phases are described in Breiter et al. (2009), Čopjaková et al. (2011) and Škoda et al. (2015). Raw intensities were reduced using the PAP matrix-correction routine (Pouchou and Pichoir 1985). X-ray element maps were acquired with a step size of 1–2 μm using a fully focused electron beam, an accelerating voltage of 15 kV, a probe current of 100 nA, and 250-500 ms/pixel dwell time.

Mineral formulae of xenotime were calculated normalized to four anions; the contents of elements in the mineral formulae are expressed in atoms per formula unit (apfu). Chemical ages were calculated according to the U-Th-total Pb-isochron method (Suzuki and Adachi 1991). Time-integrated self-irradiation doses D_α (alpha-decay events per gram) for xenotime were calculated on the basis of U and Th concentrations as determined by EPMA and the supposed crystallization age of 339±3 Ma (Novák et al. 1998), using the equation of Holland and Gottfried (1955) and Murakami et al. (1991).

Raman analysis of xenotime (performed on uncoated sample mounts) was done by means of a Horiba LabRAM HR Evolution spectrometer. This dispersive, edge filter-based system was equipped with Olympus BX-series optical microscope, a diffraction grating with 1800 grooves per millimeter, and Peltier-cooled, Si-based charge-coupled device (CCD) detector. Raman spectra were excited with the 473 nm emission of a diode laser (3 mW at the sample surface). Blue excitation was selected after careful tests with different lasers. This approach is strongly advised for xenotime–(Y) to avoid analytical artefacts, because the Raman spectrum of this mineral is well known to be widely obscured by laser-induced REE emissions (Nasdala et al., 2012; Lenz et al., 2015). With the Olympus 100× objective (numerical aperture 0.9) and the system being operated in the confocal mode, the lateral resolution was ~1 μm. Wavenumber calibration was done using the Rayleigh line and Kr lamp emissions. The wavenumber accuracy was better than 0.5 cm^{-1}, and the spectral resolution was ~1 cm^{-1}. Band fitting was done after appropriate background correction, assuming combined Lorentzian-Gaussian band shapes. Note, however, that at elevated stages of damage accumulation, Raman bands become increasingly irregular, i.e. they deviate increasingly

from symmetric shapes (Nasdala et al. 2002a). For calculated FWHM (full width at half band-maximum) values larger than ca. 15 cm^{-1}, significant uncertainties need to be considered; appropriately large errors are therefore quoted. True FWHM values were calculated by correcting the measured FWHMs for the system's apparatus function (or instrument profile function, IPF; see discussions by Nasdala et al. 2001; Presser and Glotzbach 2009), using the empirical correction formula of Váczi (2014).

Results

Textural relations and chemical compositions of xenotime–(Y)

Xenotime occurs exclusively in the albite unit of Písek pegmatites and commonly forms large, isometric, subhedral to euhedral grains (0.5–2.5 mm) of brown to green colour associated with zircon, monazite, Y,REE,Ti,Nb-oxides, tourmaline, and albite. Xenotime is characterized by considerable heterogeneity. Several different domains were distinguished on the basis of textural relations in BSE images (Fig. 2a), and EPMA data acquired from the core to the rim of xenotime grains. Textural and chemical features of xenotime are similar for all pegmatites studied.

The dominant volume fraction of xenotime is interpreted as primary in nature (Xtm I; Fig. 2b-d). It commonly consists of an euhedral, homogeneous, dark-(in BSE images) core (Xtm Ia) overgrown by a brighter zone (Xtm Ib). The intensity of BSE signal decreases continuously towards the rim where sector (Fig. 2c) or oscillatory (Fig. 2d) zoning (both Xtm Ic) is observed occasionally. In many cases, Xtm I forms subparallel intergrowths with zircon (Fig. 2b,c) or encloses anhedral to euhedral zircon grains. Primary Xtm I, corresponding to xenotime–(Y), yielded analytical totals close to 100 wt.% (98.9–101.3 wt.%) and good stoichiometry (Table 1). The total REE content, mainly HREE, is rather high (16.5–28.1 wt.% REE_2O_3; 0.18–0.31 apfu REE). Contents of U and Th are variable (0.5–6.4 wt.% UO_2, 0.00-0.05 apfu U; 0.2–4.1 wt.% ThO_2, 0.00-0.03 apfu Th) with high U/Th ratios (commonly 1.3–5.7; Fig. 3a,b). The Xtm I also shows enrichment in Zr (≤2.3 wt.% ZrO_2, ≤0.04 apfu Zr; Fig. 3c) with the highest Zr contents in the Xtm Ia core. Evolution from the chemically homogeneous Xtm Ia core with medium U and Th contents overgrown by U,Th-rich domain (Xtm Ib) with frequent zircon intergrowths is common (Fig. 2c,d). Thorium, U and Zr contents then generally decrease along with BSE intensity from the U,Th-rich intermediate domain toward the rim, although close to the rim the local sector or oscillatory zonation reflects fluctuating U and Th contents. Minor amounts of SiO_2 (0.2–3.2 wt.%, 0.01–0.11 apfu Si), CaO (≤0.7 wt.%) and F (≤0.2 wt.%) are locally present in this xenotime (Fig. 3).

Another typical textural feature of Xtm I is the presence of particularly dark-(in BSE images), heterogeneous domains of altered xenotime II (Fig. 2c,d). Following Kempe et al. (2000), who described unusually low BSE-intensity as a typical feature of secondary alteration products, we interpret the Xtm II as a product of fluid-driven alteration. Pointer et al. (1988) and Nasdala et al. (2009) have assigned the very low intensity in BSE images (which is always connected with deficient analytical totals; cf. below) to the sub-micrometer scale porosity of altered material, rather than elevated levels of low-Z elements. The Xtm II interior regions are typically spatially related to intermediate U,Th-rich Xtm Ib zones. The Xtm II is characterized by heterogeneous chemical composition, deficient analytical totals (84.1–99.2 wt.%) and non-stoichiometry (Table 1). Similar

to the low BSE, deficient totals are typical of alteration products (e.g. Törnroos 1985; Smith et al. 1991; Mathieu et al. 2001). The analytical shortfall is an artefact caused by numerous, sub-micrometer-sized pores and voids, which increase the penetration depth of the primary electron beam into the sample, loss of X-ray quanta at numerous pore boundaries, charging effects, and potentially the presence of hydrous species (Nasdala et al. 2009). Xtm II shows depletion in phosphorus (0.76–0.97 apfu). Concentrations of Th are high (2.5–9.6 wt.% ThO_2, 0.02–0.08 apfu Th) whereas U is highly variable (0.8–5.5 wt.% UO_2, 0.01–0.05 apfu), which results in low U/Th ratios (0.1–1.3; Fig. 3a,b). Xtm II shows lower REE contents (0.16–0.21 apfu), and is relatively depleted in HREE relative to Xtm I (Fig. 4a). The contents of Ca and F are high (≤6 wt.% CaO, ≤0.25 apfu Ca and 3.2 wt.% F, ≤0.42 apfu F; Fig. 3d). Moreover, high Zr (≤4.9 wt.% ZrO_2, ≤0.10 apfu Zr) (Fig. 3c), Fe (≤4.5wt.% FeO, ≤0.15 apfu Fe), As (≤2.5 wt.% As_2O_5), and Sc (≤0.3 wt.% Sc_2O_3) were commonly observed.

Most xenotime grains contain patchy regions with common micro-pores that are remarkably rich in inclusions and appear to be recrystallized. Two types of such inclusion-rich domains are distinguishable based on texture and the chemical composition of inclusions. The first type (Xtm IIIa) occurs typically along the xenotime rim or selectively along U,Th-enriched sectors or zones close to the rim (Fig. 2d,e), but sometimes extending across the entire grain, and contains numerous tiny (≤10 μm) bright-(in BSE images) inclusions of U,Th-silicates (close to intermediate coffinite-thorite compositions), cheralite, and sparse larger (≤40 μm size) inclusions of monazite-(Ce). Very few former Xtm I grains are recrystallized to Xtm IIIb whose patchy micro-texture encloses abundant small (≤25 μm size) dark-(in BSE images) inclusions, where inclusions with cheralite-zircon intermediate compositions and zircon predominate (Fig. 2f). Small relics of Xtm I are locally found in the central parts of Xtm IIIb-dominated grains. Inclusion-rich Xtm IIIb is rarely replaced by florencite-(Ce). Moreover, the altered Xtm II was locally recrystallized to form fine-grained, inclusion-free Xtm IIIc (Fig. 2c,d). Xenotime III shows uniform chemical composition independent of its textural type (Xtm IIIa,b,c; Table 1), with analytical totals close to 100 wt.% (98.6–101.1 wt.%) and regular stoichiometry. It is generally low in U (0.2–2.5 wt.% UO_2, 0.00–0.02 apfu U) and Th (0.1–1.8 wt.% ThO_2, 0.00–0.02 apfu Th), with high U/Th ratios (0.8–6.0) (Fig. 3a,b). The content of REE is uniform (0.18–0.21 apfu; Fig. 4b). The contents of CaO, SiO_2, ZrO_2, and F are very low (usually ≤0.2 wt.%) (Fig. 3c-f).

In addition to large xenotime grains with a complex texture, there exists another textural type of xenotime-(Y) (Xtm IV), which clearly postdates Xtm I-III and either fills fractures in primary monazite-(Ce) or xenotime-(Y) grains, or forms inclusions in monazite-(Ce) and Y,REE,Ti,Nb-oxides (Fig. 5). Domains of monazite-(Ce) that are rich in Xtm IV form broad “belts” (up n x 100 μm in width) along the monazite margin and fractures. The xenotime-(Y) inclusions are commonly accompanied by tiny inclusions of thorite (Fig. 5a,b). Y,REE,Ti,Nb-oxides are altered to prevailing amorphous hydrated Nb,Ti,U,Y,As,Si,P,Fe,Ca-phases, containing irregular inclusions of xenotime-(Y), columbite-(Fe), zircon, scheelite, and common clay minerals. The chemical composition of Xtm IV is characterized by rather low U (0.24–1.76 wt.% UO_2, 0.00–0.02 apfu U) and Th contents (0.10–2.45 wt.% ThO_2, 0.00–0.02 apfu Th) (Table 1; Fig. 3a,b). Xtm IV occurring in association with monazite-(Ce) tends to have lower U/Th ratios (range 0.2–1.9) compared with Xtm IV associated with Xtm I or Y,REE,Ti,Nb-oxides (U/Th = 1.7–3.0; Fig. 3b) and differ REE pattern, which shows higher contents of elements between Sm and Dy and relative depletion between Er and Lu (Fig. 4c).

Chemical dating of xenotime

Chemical ages for different textural types of xenotime were calculated according to the U-Th-total Pb isochron method (Suzuki and Adachi 1991). Xenotime I provided a well-defined isochron Th* vs. Pb with a negligible intercept of 0.0017 Pb (Fig. 6). The isochron based on 33 points yields a weighted mean age of 338±11 Ma (95 % confidence) for Xtm I. A set of 18 analyses Xtm II does not yield a reasonable isochron age. These data show a highly scattered distribution in the Th^* vs. Pb plot and calculated ages of 0–360 Ma for individual analytical spots (Fig. 6). The calculated chemical ages of Xtm IIIa,b is 328 Ma (set of 17 analyses), albeit with a very large error of ±38 Ma due to the low U, Th and Pb contents (Fig. 6). An unaltered coffinite inclusion, texturally related to the formation of Xtm IIIa, provided a chemical age close to that of Xtm I (339±11 Ma), eventhough coffinite inclusions are commonly altered.

Raman spectroscopy of xenotime–(Y)

Our Raman spectra of xenotime–(Y) were in most cases dominated by two intense bands at 985–999 cm^{-1} and 1049–1059 cm^{-1} (Fig. 7). These two bands are assigned to internal stretching vibrations of the tetrahedral PO_4 groups (A_{1g}- and B_{1g}-type modes, respectively; Giarola et al. 2011). Parameters (i.e. spectral position and FWHM) determined for the main $\nu_1(PO_4)$ band near 985–999 cm^{-1} are listed in Table 1. Primary Xtm I shows high variability in the position of its main Raman band in the range 991–998 cm^{-1} (Figs. 7, 8a). With decreasing Raman shift, the FWHM of this band increases gradually (observed range 5.5–20.3 cm^{-1}) and its intensity decreases (Fig. 8a). The A_{1g} band of homogeneous, central Xtm Ia areas containing moderate amounts of U and Th is rather broad (FWHMs 8.9–15.6 cm^{-1}), notably down-shifted (Raman shifts 993–996 cm^{-1}), and low in intensity. The Xtm Ib domains with the highest U content yielded even higher FWHMs (14.3–20.3 cm^{-1}), lower band positions (991–994 cm^{-1}), and particularly low intensities. Lower U and Th concentrations observed in Xtm Ic close to the outer rims, in contrast, are associated with Raman bands with higher intensities, narrower FWHMs (5.5–8.9 cm^{-1}), and less down-shifted positions (996–998 cm^{-1}).

Altered domains (Xtm II) yielded low-intensity Raman spectra with highly variable widths of the main A_{1g} band (FWHM values 11.8–38.0 cm^{-1}) and generally low Raman-shift values (985–995 cm^{-1}; Figs. 7, 8a). Raman spectra of the Xtm III are characterized by intense and less down-shifted bands (A_{1g} position 996–999 cm^{-1}) that are rather narrow (A_{1g} FWHM 5.0–9.5 cm^{-1}), independently of the textural subtype (Xtm IIIa,b,c, Figs. 7, 8a). Similar to the latter, xenotime IV, note that this phase was only analyzed as a filler of fractures in monazite, (Ce)] is characterized by intense and narrow, mildly down-shifted A_{1g} bands (FWHMs 6.3–6.9 cm^{-1}; position 996 cm^{-1}; Fig. 8a). The B_{1g} band (1049–1059 cm^{-1}) shows similar FWHM and Raman-shift changes as described above, changes appear less significant.

Cumulative radiation dose in xenotime

Time-integrated alpha doses, calculated from the U and Th concentrations (EPMA) and assuming a sample age 339 Ma (Novák et al. (1998) are listed in Table 1. The highest cumulative radiation dose in primary Xtm I was calculated for the U- and Th-rich domains (up to $7.40(5) \times 10^{19}$ events/gram), whereas the homogeneous core and U,Th- poor outermost rims yielded lower values

(~3.40(5) × 10^{19} events/gram and 6.1(5) × 10^{18} – 1.40(5) × 10^{19} events/gram, respectively). The decay of ^{238}U and ^{235}U has caused 85–96 % of the total alpha dose whereas the rest falls upon ^{232}Th. The altered domains (Xtm II) yielded cumulative alpha doses in a similar range (1.90(5) × 10^{19} – 7.60(5) × 10^{19} events/gram) as Xtm I, but the contribution of U to the dose decreases to 26–85 % (arithmetic mean $\bar{x}$ = 70%) and influence of Th consequently increases. For Xenotime III the lowest radiation dose was calculated (3.1(5) × 10^{18} – 2.90(5) × 10^{19}; median 8.70(5) × 10^{19} events/gram) with a variable 51–96% but generally high ($\bar{x}$ = 91%) contribution of the U to the dose. The cumulative radiation dose of Xtm IV varies within a range similar to Xtm III (3.5(5) × 10^{18} – 2.10(5) × 10^{19}; median 9.4(5) × 10^{18} events/gram) and the contribution of the U to the dose is 51–83% ($\bar{x}$ = 73%).

Considering the same uniform age (339 Ma) of all xenotime types, which is reasonable for Xtm I, but admittedly a bit disputable for Xtm II-IV, the time-integrated, cumulative radiation dose is a function of the U and Th content. The self-irradiation dose that is calculated for the time period since primary xenotime formation is however a measure for the radiation damage present only if no secondary recrystallization, thermal annealing, or other process reconstituting the structural state has occurred (for zircon discussed in detail by Nasdala et al. 2001, 2014). Our xenotime, in contrast, may be assumed to have experienced major structural reconstitution (similar to findings of Ruschel et al. 2010 for natural monazite). This is suggested by the observation that even Xtm I for which doses in the range 2–7 × 10^{19} events/gram were calculated, yielded broadened but still well-measurable Raman bands of crystalline YPO_4. Our observation is in contrast to observations of Zhang et al. (2000) and Nasdala et al. (2002b) who found that zircon is amorphised by ca. 1 × 10^{19} alpha-decay events/gram. It appears reasonable to speculate that phosphate minerals undergo a crystalline-to-amorphous transition after sustaining a similar order of self-irradiation. The latter has been supported in an ion-irradiation study of $CePO_4$ (Nasdala et al. 2010a). Note also that Xtm I shows a fairly close correlation of Raman-parameter changes with the dose (Figs. 8b and 8c) whereas data pairs for Xtm II show much larger scatter. The latter may perhaps point to secondary changes in Th and/or U, resulting in biased dose values.

Discussion

Magmatic xenotime

The textural relations and chemical composition of xenotime indicate that the large xenotime grains crystallized from melt almost simultaneously with zircon, monazite and tourmaline. The presence of the chemically homogeneous Xtm Ia core surrounded by zonal Xtm Ib (Fig. 2d) probably indicates two-phase magmatic crystallization, where Xtm Ia crystallizing from a less evolved melt was overgrown by Xtm Ib precipitating from a more evolved melt (Fig. 9). The U/Th ratio of unaltered Xtm I increases from the core towards the rim, reflecting melt evolution. Uranium and Th entered the unaltered xenotime via the $(U,Th)SiY_{-1}P_{-1}$ substitution; the coffinite component (≤5 mol% $USiO_4$) predominates over thorite (≤3 mol% $ThSiO_4$) and the cheralite substitution $CaThY_{-2}$ is insignificant (Fig. 3e,f), which is consistent with other studies of xenotime from granitic rocks (Förster 1998; Broska et al. 2005). An outward decrease in U, Th, Si and Ca is a common feature of magmatic xenotime (Broska et al. 2005; Broska and Petrík 2014).

The main A_{1g} Raman band of Xtm I (Fig. 7) showed a range of spectral parameters that seems to correlate very well with its U and Th contents and hence the calculated alpha dose (Fig. 8b,c). The spectral changes are therefore assigned to increasing structural disorder due to the increased accumulation of self-irradiation damage. Similar FWHM increases and intensity losses, often accompanied by band shifts to lower energies, have been observed for radiation-damaged zircon (Nasdala et al. 1995; Wopenka et al., 1996), monazite–(Ce) (Seydoux-Guillaume et al. 2002; Ruschel et al. 2012), cordierite (Nasdala et al. 2006), and titanite (Beirau et al. 2010).

Magmatic Xtm I is generally enriched in Zr (≤4 mol% $ZrSiO_4$), whereas recrystallized Xtm III and late-stage Xtm IV are Zr-poor. Hence, Zr could be used as a discriminator of magmatic or hydrothermal origin. It is however a puzzling observation that published analyses of xenotime include Zr only rarely. The observed elevated HREE content and significant negative Eu anomaly of Xtm I (Fig. 4a; Table 1) are consistent with findings for xenotime from other occurrences in evolved granites and pegmatites (Demartin et al. 1991; Förster 1998; Buck et al. 1999; Hetherington and Harlov 2008). The primary magmatic growth zones of Xtm I are interrupted by complex secondary textures as a result of interaction with aqueous fluids (Figs. 2c-f; 9).

Recrystallization of primary xenotime in a fluid-driven alteration process

Altered areas similar to Xtm IIIa,b (Figs. 2d,e,f, 9, 10a,b), i.e. characterized by a heterogeneous texture with patchy zoning, common micro-pores, cracks and tiny inclusions, are commonly interpreted as a result of coupled dissolution-reprecipitation processes driven by interacting fluids (Putnis 2002, 2009; Hetherington and Harlov 2008). This process proceeded from rim inwards (Fig. 9) and sometimes the whole grain was metasomatized. Two types of xenotime recrystallization have been distinguished in relation to the type of exsolved inclusions (Figs. 2d,e,f, 10a,b). More common Xtm IIIa containing tiny coffinite/thorite, cheralite and monazite (Figs. 2d,e, 10a) is interpreted as a result of reaction of the magmatic Xtm I with the H_2O-rich pegmatite-derived fluids through the process of fluid-driven alteration.

Recrystallized Xtm IIIb shows a mesh texture with Zr,Th-rich inclusions as knots of mesh-like fractures around patchy and micro-porous xenotime IIIb (Fig. 2f, 10b), which indicates a fluid-mediated alteration process as well. Different kind of inclusions, as well as slightly higher Th and Zr contents in recrystallized domains of Xtm IIIb (Table 1 compare Xtm IIIb and IIIa), can indicate higher fluid temperature responsible for this type of recrystallization. On the other hand, it could be related to primary xenotime , where the relicts of magmatic xenotime enclosed in recrystallized Xtm IIIb are Zr-, U- and Th-rich and equivalent to Xtm Ia. Moreover, the absence of subparallel intergrowths of xenotime with zircon can indicate missing evolution from Xtm Ia to XtmIb,c. In contrast, recrystallized Xtm IIIa is commonly spatially associated with the outer zones of Xtm Ic, which is rather poor in Zr, Th, and U.

Recrystallized xenotime IIIa,b is well crystalline compared to primary magmatic Xtm I and shows composition close to end-member xenotime (low U, Th, Si, and Zr; Table 1; Fig. 10a,b); however, their REE contents and patterns, as well as high U/Th ratios, are comparable (Figs. 3,4). Metasomatized xenotime from granitic pegmatites of the Hidra massif (Norway) also contains low contents of U, Th and Si (Hetherington and Harlov 2008). The calculated chemical age of Xtm III is 328 ±38 Ma, and the undisturbed U–Th–Pb system (see Fig. 6) likely represents the timing of fluid influx and mineral recrystallization.

Metasomatic alteration of Xtm I yielding altered regions of xenotime IIIa,b occurred in a semi-closed chemical system, where almost all components (except Ca) necessary for the nucleation and growth of inclusions and Xtm IIIa,b were present in the host xenotime I (Table 1; Figs. 9, 10a,b). There is a limited number of published experimental studies concerning the stability of xenotime under the conditions corresponding to post-magmatic alteration of granitic rocks and none of them yielded inclusion-rich textures similar to those observed in Xtm IIIa,b. On the other hand, texturally similar metasomatized domains in xenotime were described in nature, e.g. in granitic pegmatites of the Hidra massif where metasomatized domains of xenotime host different kinds of inclusions, thorite and uraninite (Hetherigton and Harlov 2008; Hetherington et al. 2008). In contrast, breakdown of magmatic xenotime during its interaction with metamorphic fluids, in the course of prograde metamorphism at greenschist to amphibolite facies conditions, results in the formation of different textures consisting of a xenotime relict core mantled by apatite and HREE-rich epidote rim (Broska et al. 2005; Broska and Petrík 2015), or by apatite and hingganite-(Y) rim (Majka et al. 2011). Experimental xenotime alterations commonly results in the dissolution of its surface without affecting the composition of internal domains and the releaseof Y+REE precipitated as Y,HREE-rich silicates and apatite (Hetherington et al. 2010; Budzyń and Kozub-Budzyń 2015), i.e. is similar to the processes observed in course of prograde metamorphic processes observed in nature.

Hydrothermal alteration of radiation-damaged xenotime

During the postmagmatic stage, the chemical composition of medium to poorly crystalline U,Th-rich internal xenotime domains (Xtm Ib) changed significantly to produce Xtm II as a result of xenotime interaction with low-T hydrothermal fluids (Figs. 2c,d, 9). Metasomatic alteration of Xtm I producing domains of micro-porous Xtm IIIa,b provided passageways for fluids to internal poorly crystalline U,Th-rich xenotime domains (Xtm Ib) via micro-pores. Amorphous domains and in particular the areas of low density in radiation-damaged minerals facilitated chemical transport and diffusion-reaction processes between the amorphous phase and fluid (Geisler et al. 2007). The altered domains of Xtm II accommodate high levels of Ca, F, Th, Zr, Fe, and locally also As, Sc and Ce. On the other hand, Xtm II is typically depleted in P, Y, HREE, U, Si and radiogenic Pb (Figs. 4a, 9, 10c; Table 1), indicating an open chemical system during this type of alteration. The best indicators of this alteration process in xenotime are Ca and F (Fig. 10c), which are commonly very low in unaltered domains and significantly increase in concentration with decreasing analytical total (Fig. 3d, Table 1). In contrast, altered magmatic xenotime from the Hora Svaté Kateřiny A-type granite, Czech Republic (Breiter et al. 2009), shows higher Si, As, S, F, Nb, Ta, W, Sc, Bi, Fe and Ca contents, coupled with reduced HREE and P levels. Similar secondary chemical changes are known for radiation-damaged zircon. Incorporation of solvent cations (mainly Al and Ca, F, Fe with minor Y, Ba, Mg, Sc, Nb, Bi and As) from a solution into radiation-damaged zircon and its depletion in Zr, Hf, Si and radiogenic Pb have been reported by many workers (Sinha et al. 1992; Geisler and Schleicher 2000; Geisler et al. 2002, 2003a,b; Breiter et al. 2009; Nasdala et al. 2009, 2010b; Förster et al. 2011). Moreover, LREE enrichment has been reported for hydrothermally altered zircon (Hoskin 2005; Horie et al. 2006; Hönig et al. 2014). The presence of substituent elements in the altered domains of radiation-damaged xenotime or zircon depends significantly on the cations present in alteration fluids; however, the Ca content seems to be the best chemical proxy for alteration of zircon (Geisler and Schleicher 2000) and xenotime. Yttrium and HREE from

radiation-damaged xenotime were mobilized by F-rich low-T hydrothermal fluids. Numerous natural examples across a range of geological conditions, as well as experimental data, document the mobility of Y+REE and their fractionation in a F-rich environment (e.g. Wood 1990; Pan and Fleet 1996; Broska et al. 2005).

In our case, the U/Th ratio was affected by the xenotime alteration, decreasing significantly from 1.3–2.6 in unaltered Xtm Ib to 0.1–1.3 in the altered Xtm II domains. Irregular relationships between the cumulative dose, FWHM and Raman-shift values (Fig. 8b,c) indicate that the U–Th system was not closed during the alteration processes; this is also indicated by the changes in U/Th ratio. Without changes in U and Th, we would have expected a close positive correlation between the cumulative dose and FWHM (and Raman-shift values, respectively) along the regression trend for Xtm I, which, however, is not observed. Based on our EPMA results (Table 1) and X-ray distribution maps (Fig. 10c), the decreasing U/Th ratios reflect Th enrichment and U depletion in the altered domains compared with surrounding unaltered domains, which is interpreted as a result of xenotime alteration. Perhaps, U was easily mobilized by oxidizing hydrothermal fluids. Thorium, which is significantly enriched in altered xenotime domains, was probably released during the fluid-driven alteration of xenotime (Xtm I→Xtm IIIa,b) or as a result of alteration of metamict Th-rich minerals (thorite, cheralite). Zircon did not show any significant changes in Th content during alteration of its metamict domains (authors' unpublished data). Geisler and Schleicher (2000) reported U and Th enrichment in naturally altered domains, whereas U and Th depletion was observed in leaching experiments on altered zircon (Geisler et al. 2002, 2003b).

Interaction of radiation-damaged xenotime with hydrothermal fluids resulted in disturbance of the U–Th–Pb system, which must be taken in account when interpreting the geochronological data. As a consequence, the calculated Th–U–Pb ages of Xtm II do not form an isochron and show much scattering in the Pb vs. Th^{*} plot compared to the chemical age of Xtm I (338±11 Ma) yielding a well-defined isochron (Fig. 6) and agreeing with the isotopic U/Pb age of monazite (339±3 Ma; Novák et al. 1998). Similar fluid-induced disturbance of the U–Th–Pb isotope system was described for altered zircon domains (Nasdala et al. 1998, 2010b; Geisler and Schleicher 2000; Geisler et al. 2002, 2003b; Schmidt et al. 2006).

Nucleation and growth of tiny Xtm IIIc grains as a result of interaction of altered domains (Xtm II) with hydrothermal fluids was locally observed (Figs. 2c,d, 9, 10c). Geisler et al. (2003b) revealed that kinetics of structural recovery of metamict zircon is significantly enhanced by the presence of water compared to “dry” conditions. In spite of the very fine-grained character of Xtm IIIc (Fig. 2c,d), it is well distinguished from surrounding altered, amorphous Xtm II due to its well crystalline nature (Fig. 7) and different chemistry close to $(Y,REE)PO_4$ (Table 1; Fig. 10c) with low U and Th and a high U/Th ratio. Xtm IIIc is similar in chemical composition to hydrothermally recrystallized Xtm IIIa,b (Fig. 3), but contrary to the latter, is inclusion-free.

Other types of post-magmatic xenotime formation

Several other types of post-magmatic xenotime were distinguished and described as Xtm IV(Fig. 5). Other REE-bearing minerals (monazite and Y,REE,Ti,Nb-oxides) were unstable during the fluid-induced overprinting. Small xenotime inclusions formed as a consequence of fluid-driven alteration during interaction between the magmatic monazite or Y,REE,Ti,Nb-oxides with pegmatite-derived fluids. The formation of post-magmatic xenotime inclusions as a result of the fluid-driven alteration of magmatic zircon or apatite was reported by Harlov (2011) and Broska and

Petrík (2014). The xenotime filling fractures in the magmatic monazite and/or xenotime crystallized from hydrothermal fluids as well.
Secondary Xtm IV is well crystalline and differs from magmatic Xtm I by its low U, Th and Zr contents (Fig. 3a-c). Generally, it is similar to Xtm III, but there are some specific differences linked to the precursor mineral. Differences in the chemical composition of secondary Xtm IV associated with monazite (enriched in REE from La to Dy and poorer in REE from Er to Lu; higher Th contents resulting in lower U/Th ratios) compared to the other textural varieties of Xtm IV (Figs. 3a,b, 4c), indicate short-range transport of REE and Th by hydrothermal fluids and significant effect of the chemical composition of the precursor phase (monazite, xenotime, or Y,REE,Ti,Nb-oxides) on the chemical composition of secondary xenotime.

Nature, chemistry and temperature of fluids

Complex secondary textures cutting magmatic Xtm I and the formation of Xtm II-IV are interpreted as a result of interaction of primary magmatic minerals with H_2O-rich pegmatite-derived fluids. Field observations did not reveal any evidence of regional metamorphism or deformation of pegmatite and therefore the involvement of external metamorphic fluids is improbable. Moreover, an unaltered coffinite inclusion, texturally related to the formation of Xtm IIIa, gave a chemical age (339±11 Ma) indicating that Xtm I recrystallized during or shortly after solidification of the melt in the presence of melt-derived fluids. A similar observation on recrystallized xenotime in pegmatites was made by Hetherington et al. (2008). Based on the chemical composition of minerals and their assemblage, the pegmatite-derived fluids contained F, Ca and alkali elements. The alkaline character of fluids is consistent with the partial replacement of associated tourmaline by K-feldspar, muscovite and chlorite. Tourmaline (schorl-dravite) is a very stable mineral in aqueous systems (London 2011), excluding alkaline, B-undersaturated fluids, which are responsible for its breakdown (Ahn and Buseck 1998; London 2011; Čopjaková et al. 2015). The instability of xenotime in the presence of alkali fluids was documented in nature (Hetherington and Harlov 2008), as well as in experimental works (Budzyń and Kozub-Budzyń 2015).

Temperature conditions for the secondary alteration of magmatic xenotime/monazite yielding similar inclusion-rich textures such as those observed in Xtm IIIa,b have not been ascertained yet. Experimental metasomatic alteration of REE-rich apatite producing similar textures and involving the development of monazite and xenotime inclusions covers a wide range of temperatures (300-900°C) and is mainly a function of the fluid composition (Harlov et al. 2002, 2005). The upper temperature stability limit for florencite in metapelites is 350 °C (Rasmussen 1996; Janots et al. 2006). Thus, the process where florencite-(Ce) locally replaces the already recrystallized xenotime had to occur at T < 350 °C.

Textural relations indicate that the alteration process that formed Xtm IIIa,b preceded the alteration of radiation-damaged xenotime domains and formation of Xtm II. The recrystallized areas contain abundant micro-pores facilitating access of fluids (Putnis 2002, 2009) to the inner U,Th-rich, radiation-damaged xenotime zones. We assume that the intensive alteration of radiation-damaged xenotime (responsible for Xtm II domains) started at temperatures >200 °C, because the altered areas (Xtm II) are commonly recrystallized to Xtm IIIc. In experiments, massive recrystallization of radiation-damaged zircon occurs at temperatures in the range 200-350 ºC depending on fluid chemistry (Geisler et al. 2003b,c; Schmidt et al. 2006). The presence of Fe-rich

kaolinite, kahlerite, and pharmacosiderite in the fracture-filling mineral assemblage in xenotime, monazite, and Y,REE,Ti,Nb-oxides of the Písek pegmatites (Škoda et al. 2011) suggests protracted alteration of metamict minerals and mobilization of U with temperatures decreasing below 150-200 °C, i.e. to the stability field of clay minerals and pharmacosiderite (Dekov et al. 2008; Drahota and Filippi 2009).

Conclusions

Our study shows that a combination of textural, chemical and structural observations is needed to understand the complex formation and alteration history of xenotime from the Písek pegmatites. In particular, U, Th, Si, HREE, Zr, Ca and F substituting in xenotime were found to provide valuable information on its evolutionary history. Raman spectroscopic parameters correlate well with U+Th concentrations, which is assigned to increasing structural disorder due to the increased accumulation of self-irradiation damage.

At Písek, large xenotime grains enriched in U, Th and Zr crystallized directly from the melt, simultaneously with zircon, monazite and tourmaline. In a late formation stage, the xenotime grains were altered by interaction with melt-derived fluids rich in F, Ca and alkali elements, and the magmatic xenotime was recrystallized. This complex process resulted in the formation of inclusion-rich xenotime domains with composition close to the end-member and several types of inclusions (cheralite-zircon intermediate compositions + zircon, or coffinite-thorite + cheralite + monazite).

The secondary alteration of xenotime resulted in the formation of a micro-porous texture that facilitated the access of fluids, which in turn resulted in intensive alteration of the inner radiation-damaged xenotime zones. This process probably started at temperatures well above 200 °C. It resulted in the formation of newly grown and hence crystalline xenotime, whose chemical composition, however, deviates significantly from that of the initial material, reflecting depletion in P, Y, HREE, U, Si and radiogenic Pb, accompanied by enrichment in Ca, F, Th, Zr, Fe. Disturbance of the U–Th–Pb system caused by the interaction of the xenotime with hydrothermal fluids (especially if the xenotime were susceptible to chemical attack due to the accumulation of radiation damage) must be taken in account when interpreting geochronological data.

Acknowledgements The samples investigated in this study were kindly provided from the mineral collection of the Prácheň Museum in Písek. This work was supported within EU project “Research group for radioactive waste repository and nuclear safety” (CZ.1.07/2.3.00/20.0052) to Z.L. and R.Š. R.C. acknowledges support within the research programme MUNI/A/1451/2014 of Masaryk University, and L.N. funding by the Austrian Science Fund (FWF) through project no. P244481–N19. We thank reviewers Igor Broska and Martin Ondrejka and Associate editor Anton Chakhmouradian for their constructive comments, which helped to significantly improve the quality of this paper.

References

Ahn JH, Buseck PR (1998) Transmission electron microscopy of muscovite alteration of tourmaline. Am Mineral 83:535-541

Åmli R (1975) Mineralogy and rare earth geochemistry of apatite and xenotime from the Gloserheia granite pegmatite, Froland, southern Norway. Am Mineral 60:607–620

Bea F (1996) Residence of REE, Y, Th and U in granites and crustal protoliths; implications for the chemistry of crustal melts. J Petrol 37:521–552

Beirau T, Bismayer U, Mihailova B, Paulmann C, Groat L (2010) Structural phenomena of metamict titanite: a synchrotron, X-ray diffraction and vibrational spectroscopic study. Phase Transit 83:694–702

Bernhard F, Walter F, Ettinger K, Taucher J, Mereiter K (1998) Pretulite, $ScPO_4$, a new scandium mineral from the Styrian and Lower Austrian lazulite occurrences, Austria. Am Mineral 83:625–630

Bouška V, Johan Z (1972) New data on písekite. Lithos 5:93–103

Breiter K, Čopjaková R, Škoda R (2009) The involvement of F, CO_2, and As in the alteration of Zr-Th-REE-bearing accessory minerals in the Hora Svaté Kateřiny A-type granite, Czech Republic. Can Mineral 47:1375–1398

Broska I, Petrík I (2014) Accessory phases in the genesis of the igneous rocks. In: Kumar S, Singh RN (eds) Modelling of magmatic and allied processes. Soc Earth Sci, Ser, vol 83. Springer, Berlin, pp 109–149

Broska I, Petrík I (2015) Variscan thrusting in I- and S-type granitic rocks of the Tribeč Mountains, Western Carpathians (Slovakia): evidence from mineral compositions and monazite dating. Geol Carpath 66:455–471

Broska I, Williams CT, Janák M, Nagy G (2005) Alteration and breakdown of xenotime-(Y) and monazite-(Ce) in granitic rocks of the Western Carpathians, Slovakia. Lithos 82:71–83

Buck HM, Cooper MA, Černý P, Grice JD, Hawthorne (1999) Xenotime-(Yb), $YbPO_4$, a new mineral species from the Shatford Lake pegmatite group, southeastern Manitoba, Canada. Can Mineral 37:1303–1306

Budzyń B, Kozub-Budzyń GA (2015) The stability of xenotime in high Ca and Ca-Na systems, under experimental conditions of 250-350 ^{o}C and 200-400 MPa: the implications for fluid-mediated low-temperature processes in granitic rocks. Geol Quart 59:316–324

Cícha J, Houzar S, Litochleb J, Novák M (2005) Excursion guidebook for mineralogical and geological localities (in Czech). Feldspar 2005: The Workshop of geologists from the Czech and Slovak museums, Prácheň Museum in Písek, 50 p

Čopjaková R, Novák M, Franců E (2011) Formation of authigenic monazite-(Ce) to monazite-(Nd) from Upper Carboniferous graywackes of the Drahany Upland: Roles of the chemical composition of host rock and burial temperature. Lithos 127:373–385

Čopjaková R, Škoda R, Vašinová Galiová M, Novák M, Cempírek J (2015) Scandium- and REE-rich tourmaline replaced by Sc-rich REE-bearing epidote-group mineral from the mixed (NYF + LCT) Kracovice pegmatite (Moldanubian Zone, Czech Republic). Am Mineral 100:1434-1451

Dekov VM, Caudros J, Shanks WC, Koski RA (2008) Deposition of talc - kerolite-smectite - smectite at seafloor hydrothermal vent fields: evidence from mineralogical, geochemical and oxygen isotope studies. Chem Geol 247:171-194

Demartin F, Pilati T, Diella V, Donzelli S, Gentile P, Gramaccioli CM (1991) The chemical composition of xenotime from fissures and pegmatites in the Alps. Can Mineral 29:69–75

Drahota P, Filippi M (2009) Secondary arsenic minerals in the environment: a review. Environ Int 35:1243–1255

Ewing RC (1976) Metamict mineral alteration: An implication for radioactive waste disposal. Science 192:1336–1337

Ewing RC (1994) The metamict state: 1993 - the centennial. Nucl Instrum Meth B 91:22–29

Ewing RC (2007) Ceramic matrices for plutonium disposition. Prog Nucl Energ 49:635–643

Ewing RC, Weber WJ (2010) Actinide waste forms and radiation effects. In: Morss LR, Edelstein NM, Fuger J (eds) The chemistry of the actinide and transactinide elements, vol 6. Springer, New York, pp 3813-3888

Fišera M (2000) Geological Map of the Czech Republic 1:50 000. Sheet 22-41 Písek. Czech Geol Survey, Prague

Förster HJ (1998) The chemical composition of REE-Y-Th-U-rich accessory minerals in peraluminous granites of the Erzgebirge-Fichtelgebirge region, Germany: Part II. Xenotime. Am Mineral 83:1302–1315

Förster HJ, Ondrejka M, Uher P (2011) Mineralogical responses to subsolidus alteration of granitic rocks by oxidizing As-bearing fluids: REE arsenates and As-rich silicates from the Zinnwald granite, Eastern Erzgebirge, Germany. Can Mineral 49, 4:913-930

Franke W (2000) The mid-European segment of the Variscides: tectono-stratigraphic units, terrane boundaries and plate tectonic evolution. In: Franke W, Haak V, Oncken O, Tanner D (eds) Orogenic Processes: Quantification and modelling in the Variscan Belt. Geol Soc Spec Publ 179, pp 35–62

Geisler T, Schleicher H (2000) Improved U-Th-total Pb dating of zircons by electron microprobe using a simple new background modeling procedure and Ca as a chemical criterion of fluid-induced U-Th-Pb discordance in zircon. Chem Geol 163:269-285

Geisler T, Pidgeon RT, van Bronswijk W, Kurtz R (2002) Transport of uranium, thorium, and lead in metamict zircon under low-temperature hydrothermal conditions. Chem Geol 191:141–154

Geisler T, Rashwan AA, Rahn MKW, Poller U, Zwingmann H, Pidgeon RT, Schleicher H, Tomaschek F (2003a) Low-temperature hydrothermal alteration of natural metamict zircons from the Eastern Desert, Egypt. Mineral Mag 67:485–508

Geisler T, Pidgeon RT, Kurtz R, van Bronswijk W, Schleicher H (2003b) Experimental hydrothermal alteration of partially metamict zircon. Am Mineral 88:1496-1513

Geisler T, Zhang M, Salje EKH (2003c) Recrystallization of almost fully amorphous zircon under hydrothermal conditions: An infrared spectroscopic study. J Nucl Mater 320:280–291

Geisler T, Schaltegger U, Tomaschek F (2007) Re-equilibration of zircon in aqueous fluids and melts. Elements 3:43–50

Giarola M, Sanson A, Rahman A, Mariotto G, Bettinelli M, Speghini A, Cazzanelli E (2011) Vibrational dynamics of YPO_4 and $ScPO_4$ single crystals: An integrated study by polarized Raman spectroscopy and first-principles calculations. Phys Rev B 83:224302

Gratz R, Heinrich W (1997) Monazite-xenotime thermobarometry: Experimental calibration of the miscibility gap in the binary system $CePO_4$-YPO_4. Am Mineral 82:772–780

Harlov DE (2011) Formation of monazite and xenotime inclusions in fluorapatite megacrysts, Gloserheia Granite Pegmatite, Froland, Bamble Sector, southern Norway. Mineral Petrol 102:77–86

Harlov DE, Förster H-J, Nijland TG (2002) Fluid induced nucleation of (Y+REE)-phosphate minerals within apatite: Nature and experiment. Part I. Chlorapatite. Am Mineral 87:245–261

Harlov DE, Wirth R, Förster H-J (2005) An experimental study of dissolution-reprecipitation in fluorapatite: fluid infiltration and the formation of monazite. Contrib Mineral Petrol 150:268–286

Hetherington CJ, Harlov DE (2008) Metasomatic thorite and uraninite inclusions in xenotime and monazite from granitic pegmatites, Hidra anorthosite massif, southwestern Norway: Mechanics and fluid chemistry. Am Mineral 93:806–820

Hetherington CJ, Jercinovic MJ, Williams ML, Mahan K (2008) Understanding geologic processes with xenotime: Composition, chronology, and a protocol for electron probe microanalysis. Chem Geol 254:133–147

Hetherington CJ, Harlov DE, Budzyń B (2010) Experimental metasomatism of monazite and xenotime: mineral stability, REE mobility and fluid composition. Mineral Petrol 99:165–184

Holland HD, Gottfried D (1955) The effect of nuclear radiation on the structure of zircon. Acta Crystallogr 8:291–300

Holub FV (1997) Ultrapotassic plutonic rocks of the durbachite series in the Bohemian Massif: Petrology, geochemistry and petrogenetic interpretation. Sbor geol Věd, ložisk Geol Mineral 31:5–26. Prague

Hönig S, Čopjaková R, Škoda R, Novák M, Dolejš D, Leichmann J, Vašinová Galiová M (2014) Garnet as a major carrier of the Y and REE in the granitic rocks: An example from the layered anorogenic granite in the Brno Batholith, Czech Republic. Am Mineral 99:1922–1941

Horie K, Hidaka H, Gauthier-Lafaye F (2006) Elemental distribution in zircon: Alteration and radiation-damage effects. Phys Chem Earth 31:587–592

Hoskin PWO (2005) Trace-element composition of hydrothermal zircon and the alteration of Hadean zircon from the Jack Hills, Australia. Geochim Cosmochim Acta 69:637–648

Janots E, Negro F, Brunet F, Goffe B, Engi M, Bouybaouène ML (2006) Evolution of the REE mineralogy in HP-LT metapelites of the Sebtide complex, Rif, Morocco: monazite stability and geochronology. Lithos 87:214–234

Janoušek V, Holub FV (2007) The causal link between HP-HT metamorphism and ultrapotassic magmatism in collisional orogens: case study from the Moldanubian Zone of the Bohemian Massif. Proceed Geol Assoc 118:75–86

Janoušek V, Finger F, Roberts MP, Frýda J, Pin C, Dolejš D (2004) Deciphering the petrogenesis of deeply buried granites: whole-rock geochemical constraints on the origin of largely undepleted felsic granulites from the Moldanubian Zone of the Bohemian Massif. Trans Roy Soc Edin-Earth 95:141–159

Janoušek V, Vrána S, Erban V, Vokurka K, Drábek M (2008) Metabasic rocks in the Varied Group of the Moldanubian Zone, southern Bohemia - their petrology, geochemical character and possible petrogenesis. J Geosci 53:31–46

Kempe U, Gruner T, Nasdala L, Wolf D (2000) Relevance of cathodoluminescence for the interpretation of U-Pb zircon ages, with an example of an application to a study of zircons

from the Saxonian Granulite Complex, Germany. In: Pagel M, Barbin V, Blanc P, Ohnenstetter D (eds) Cathodoluminescence in Geosciences. Springer, Berlin, Heidelberg, New York, pp 415–455

Kotková J (2007) High-pressure granulites of the Bohemian Massif: recent advances and open questions. J Geosci 52:45–71

Lenz C, Nasdala L, Talla D, Hauzenberger C, Seitz R, Kolitsch U (2015) Laser-induced REE^{3+} photoluminescence of selected accessory minerals – An "advantageous artefact" in Raman spectroscopy. Chem Geol 415:1–16

London D (2011) Experimental syntesis and stability of tourmaline: a historical overview. Can Mineral, 49:117-136

Majka J, Pršek J, Budzyń B, Bačík P, Barker A, Lodzinski M (2011) Fluorapatite-hingganite-(Y) coronas as products of fluid induced xenotime-(Y) breakdown in the Skoddefjellet pegmatite (Svalbard). Mineral Mag 75:159-167

Mathieu R, Zetterström L, Cuney M, Gauthier-Lafaye F, Hidaka H (2001) Alteration of monazite and zircon and lead migration as geochemical tracers of fluid paleocirculations around the Oklo-Okélobondo and Bangombé natural nuclear reaction zones (Franceville basin, Gabon). Chem Geol 171:147–171

Medaris LG Jr, Beard BL, Johnson CM, Valley JW, Spicuzza MJ, Jelínek E, Mísař Z (1995) Garnet pyroxenite and eclogite in the Bohemian Massif: geochemical evidence for Variscan recycling of subducted lithosphere. Geol Rundsch 84:489–505

Medaris, G Jr, Wang H, Jelínek E, Mihaljevič M, Jakeš P (2005) Characteristics and origins of diverse Variscan peridotites in the Gföhl Nappe, Bohemian Massif, Czech Republic. Lithos 82:1–23

Murakami T, Chakoumakos BC, Ewing RC, Lumpkin GR, Weber WJ (1991) Alpha-decay event damage in zircon. Am Mineral 76:1510–1532

Nasdala L, Irmer G, Wolf D (1995) The degree of metamictization in zircon: a Raman spectroscopic study. Eur J Mineral 7:471–478

Nasdala L, Pidgeon RT, Wolf D, Irmer G (1998) Metamictization and U-Pb isotopic discordance in single zircons: a combined Raman microprobe and SHRIMP ion probe study. Mineral Petrol 62:1–27

Nasdala L, Wenzel M, Vavra G, Irmer G, Wenzel T, Kober B (2001) Metamictisation of natural zircon: Accumulation versus thermal annealing of radioactivity-induced damage. Contrib Mineral Petrol 141:125–144

Nasdala L, Irmer G, Jonckheere R (2002a) Radiation damage ages: Practical concept or impractical vision? - Reply to two comments on “Metamictisation of natural zircon: Accumulation versus thermal annealing of radioactivity-induced damage”, and further discussion. Contrib Mineral Petrol 143:758–765

Nasdala L, Lengauer CL, Hanchar JM, Kronz A, Wirth R, Blanc P, Kennedy AK, Seydoux-Guillaume A-M (2002b) Annealing radiation damage and the recovery of cathodoluminescence. Chem Geol 191:121–140

Nasdala L, Wildner M, Wirth R, Groschopf N, Pal DC, Möller A (2006) Alpha particle haloes in chlorite and cordierite. Miner Petrol 86:1–27

Nasdala L, Kronz A, Wirth R, Váczi T, Pérez-Soba C, Willner A, Kennedy AK (2009) Alteration of radiation-damaged zircon and the related phenomenon of deficient electron microprobe totals. Geochim Cosmochim Ac 73:1637–1650

Nasdala L, Grötzschel R, Probst S, Bleisteiner B (2010a) Irradiation damage in monazite ($CePO_4$): an example to establish the limits of Raman confocality and depth resolution. Can Mineral 48:351–359

Nasdala L, Hanchar JM, Rhede D, Kennedy AK, Váczi T (2010b) Retention of uranium in complexly altered zircon: An example from Bancroft, Ontario. Chem Geol 269:290–300

Nasdala L, Beyssac O, Schopf JW, Bleisteiner B (2012) Application of Raman-based images in the Earth sciences. In: Zoubrir A (ed) Raman imaging – Techniques and applications. Springer Series Opti, vol 168. Springer, Berlin, Heidelberg, pp 145–187

Nasdala L, Kostrovitsky S, Kennedy AK, Zeug M, Esenkulova SA (2014) Retention of radiation damage in zircon xenocrysts from kimberlites, Northern Yakutia. Lithos 206–207:252–261

Ni Y, Hughes JM, Mariano AN (1995) Crystal chemistry of the monazite and xenotime structures. Am Mineral 80:21–26

Novák M, Cícha J (2009) The classification of granitic pegmatites of the Písek region (in Czech). Mineral Special vol:8–19

Novák M, Černý P, Kimbrough DL, Taylor MC, Ercit TS (1998) U-Pb ages of monazite from granitic pegmatites in the Moldanubian Zone and their geological implications. Acta Univ Carol, Geol 42:309–310

Pabst A (1952) The metamict state. Am Mineral 37:137–157

Pan Y, Fleet ME (1996) Rare earth element mobility during prograde granulite facies metamorphism: Significance of fluorine. Contrib Mineral Petrol 123:251–262

Pointer CM, Ashworth JR, Ixer, RA (1988) The zircon-thorite mineral group in metasomatized granite, Ririwai, Nigeria. 1. Geochemistry and metastable solid solution of thorite and coffinite. Mineral Petrol 38:245–262

Pouchou JL, Pichoir F (1985) "PAP" procedure for improved quantitative microanalysis. Microbeam Anal 20:104–105

Presser V, Glotzbach C (2009) Metamictization in zircon: Raman investigation following a Rietveld approach. Part II: Sampling depth implication and experimental data. J Raman Spectrosc 40:499–508

Putnis A (2002) Mineral replacement reactions: from macroscopic observations to microscopic mechanisms. Mineral Mag 66:689–708

Putnis A (2009) Mineral replacement reactions. In: Putirka KD, Tepley FJ (eds) Minerals, Inclusions and Volcanic Processes. Rev Mineral Geochem, vol 70. Mineral Soc Am, Chantilly, pp 87–124

Rasmussen B. (1996) Early-diagenetic REE-phosphate minerals (florencite, crandallite, gorceixite and xenotime) in marine sandstones: A major sink for oceanic phosphorus, Am J Sci 296:601-632

Ruschel K, Nasdala L, Kronz A, Hanchar JM, Többens DM, Škoda R, Finger F, Möller A (2012) A Raman spectroscopic study on the structural disorder of monazite-(Ce). Mineral Petrol 105:41–55

Seydoux-Guillaume AM, Wirth R, Nasdala L, Gottschalk M, Montel JM, Heinrich W (2002) An XRD, TEM and Raman study of experimentally annealed natural monazite. Phys Chem Miner 29:240–253

Schmidt C, Rickers K, Wirth R, Nasdala L, Hanchar JM (2006) Low-temperature Zr mobility: An in situ synchrotron-radiation XRF study of the effect of radiation damage in zircon on the element release in H_2O + HCl ± SiO_2 fluids. Am Mineral 91:1211–1215

Schulmann K, Konopásek J, Janoušek V, Lexa O, Lardeaux JM, Edel JB, Štípská P, Ulrich S (2009) An Andean type Palaeozoic convergence in the Bohemian Massif. CR Geosci 341:266–286

Sinha AK, Wayne DM, Hewitt DA (1992) The hydrothermal stability of zircon: Preliminary experimental and isotopic studies. Geochim Cosmochim Ac 56:3551–3560

Škoda R, Novák M, Cícha J (2011) Uranium-niobium-rich alteration products after "písekite", an intimate mixture of Y,REE,Nb,Ta,Ti-oxide minerals from the Obrázek I pegmatite, Písek, Czech Republic. J Geosci 56:317–325

Škoda R, Plášil J, Jonsson E, Čopjaková R, Langhof J, Vašinová Galiová M (2015) Redefinition of thalénite-(Y) and discreditation of fluorthalénite-(Y): a re-investigation of type material from the Österby pegmatite, Dalarna, Sweden, and from additional localities. Mineral Mag 79:965-983

Smith DGW, de St Jorre L, Reed SJB, Long JVP (1991) Zonally metamictized and other zircons from Thor Lake, Northwest Territories. Can Mineral 29:301–309

Suzuki K, Adachi M (1991) Precambrian provenance and Silurian metamorphism of the Tsubonasawa paragneiss in the South Kitakami terrane, Northwest Japan, revealed by the chemical Th-U-total Pb isochron ages of monazite, zircon and xenotime. Geochem J 25:357–376

Talla D, Beran A, Škoda R, Losos Z (2011) On the presence of OH defects in the zircon-type phosphate mineral xenotime, (Y,REE)PO_4. Am Mineral 96:1799–1808

Taylor SR, McLennan SM (1985) The continental crust: its composition and evolution. Blackwell Scientific Publications, Oxford, 312 p

Timmerman MJ (2008) Palaeozoic magmatism. In: McCann T (ed) The Geology of Central Europe. Volume 1: Precambrian and Palaeozoic. Geological Society, London, pp 665–748

Tomašić N, Bermanec V, Gajović A, Linarić MR (2008) Metamict minerals: An insight into a relic crystal structure using XRD, Raman spectroscopy, SAED and HRTEM. Croat Chem Acta 81:391–400

Törnroos R (1985) Metamict zircon from Mozambique. Bull Geol Soc Finland 57:181–195

Váczi T (2014) A new, simple approximation for the deconvolution of instrumental broadening in spectroscopic band profiles. Appl Spectrosc 68:1274–1278

Vernilli F, Vernilli DC, Ferreira B, Silva G (2007) Characterization of a rare earth oxide obtained from xenotime mineral. Mater Charact 58:1–7

Whitney DL, Evans BW (2010) Abbreviations for names of rock-forming minerals. Am Mineral 95:185–187

Wood SA (1990) The aqueous geochemistry of the rare-earth elements and yttrium 2. Theoretical predictions of speciation in hydrothermal solutions to 350 °C at saturation water vapour pressure. Chem Geol 88:99-125

Wopenka B, Jolliff BL, Zinner E, Kremser DT (1996) Trace element zoning and incipient metamictization in a lunar zircon: Application of three microprobe techniques. Am Mineral 81:902–912

Žák J, Verner K, Janoušek V, Holub FV, Kachlík V, Finger F, Hajná J, Tomek F, Vondrovic L, Trubač J (2014) A plate-kinematic model for the assembly of the Bohemian Massif constrained by structural relationships around granitoid plutons. In: Schulmann K, Martínez Catalán JR, Lardeaux JM, Janoušek V, Oggiano G (eds) The Variscan orogeny: extent,

timescale and the formation of the European crust. Geol Soc Spec Publ 405, London, pp 169–196

Zhang M, Salje EKH, Farnan I, Graeme-Barber A, Daniel P, Ewing RC, Clark AM, Lennox H (2000) Metamictization of zircon: Raman spectroscopic study. J Phys Condens Mat 12:1915–1925

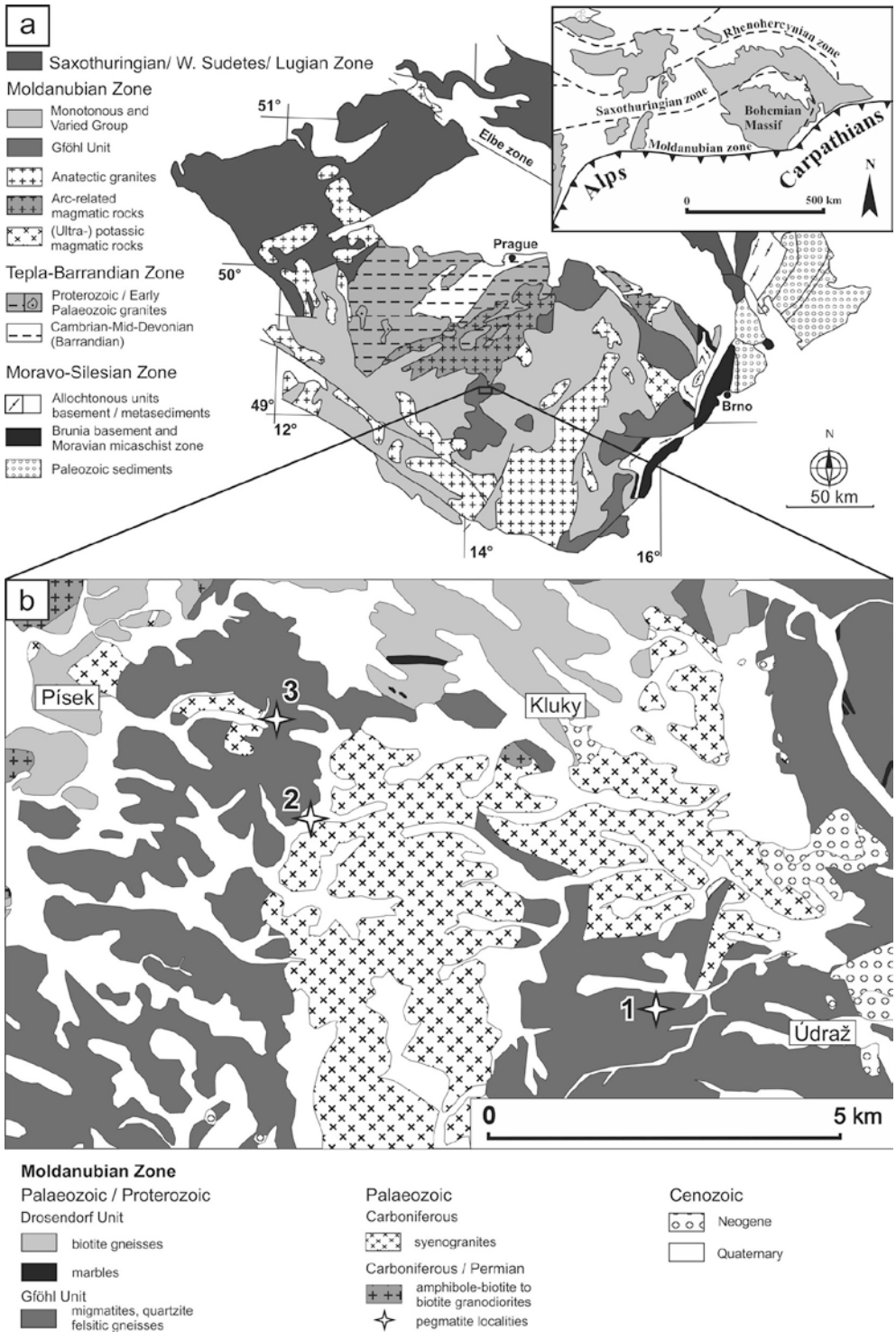

Fig. 1 Geological setting of the Písek pegmatites: **a** schematic geological map of the Bohemian Massif and its position within the European Variscides (modified after Franke 2000, Schulmann et al. 2009); **b** simplified geological map (1:50 000) of the Písek region (Fišera 2000) showing the position of pegmatite localities: 1 – Obrázek I (N 49º 18' 35.2", E 014º 11' 52.8"); 2 – U Nového rybníka (N 49º 18' 05.8", E 014º 12' 11.4"); 3 – U Údražského obrázku (N 49º 16' 51.9", E 014º 16' 36.6")

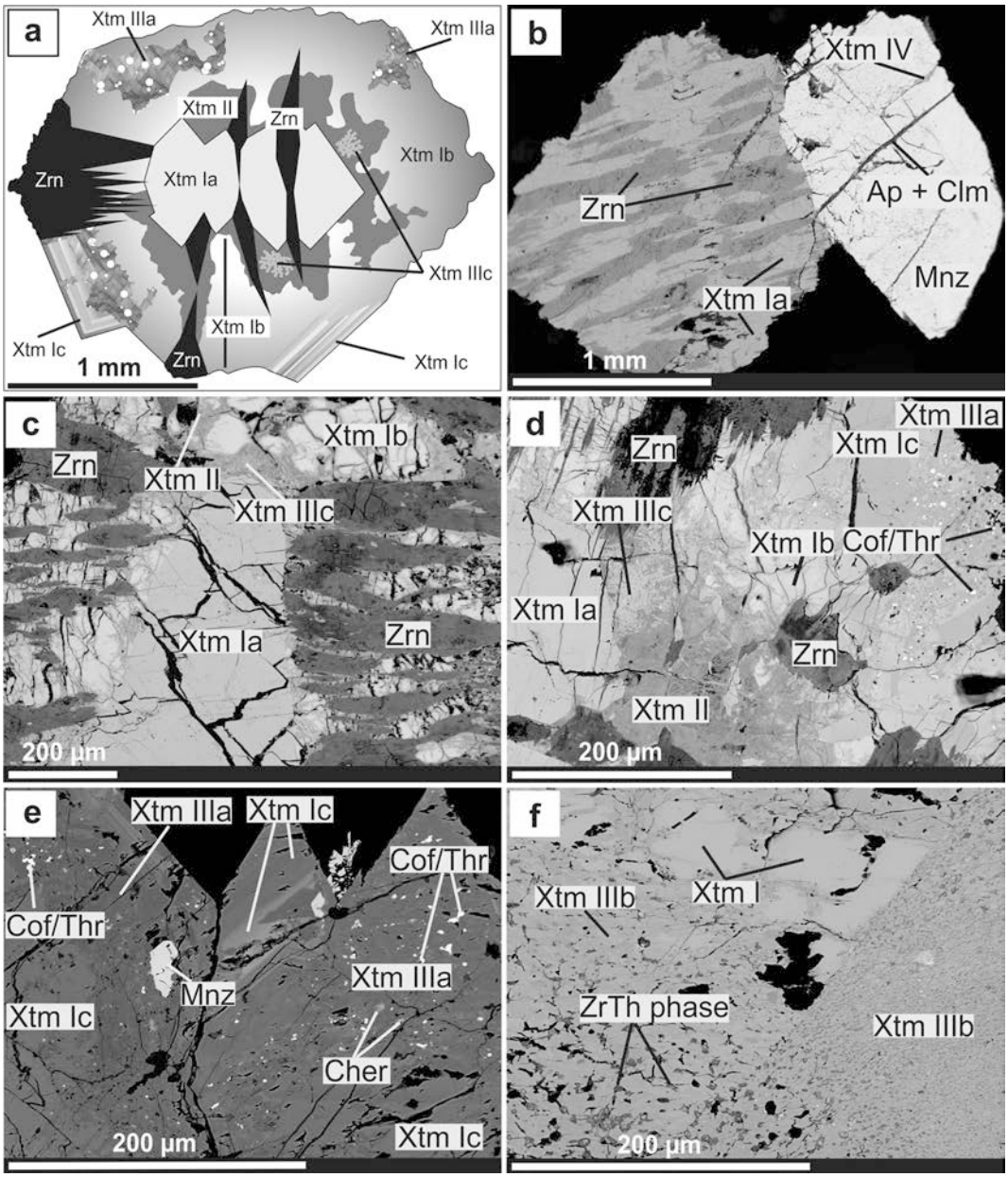

Fig. 2 Schematic sketch (**a**) and BSE images (**b**–**f**) of different xenotime-(Y) domains. **b** subhedral primary xenotime (Xtm I) intergrown with zircon; fissures in monazite are filled with xenotime IV, apatite and clay minerals; **c** xenotime with dark-BSE core (Xtm Ia) overgrown by a brighter zone (Xtm Ib) with dark altered domains (Xtm II) and inclusion-free recrystallized Xtm IIIc; **d** xenotime core (Xtm Ia) overgrown by brighter intermediate domain (Xtm Ib) accompanied by dark altered Xtm II with fine-grained recrystallized inclusion-free Xtm IIIc; near the rim, sector zoning (Xtm Ic) with recrystallization (Xtm Ic → Xtm IIIa) of originally U,Th-enriched sectors is visible; **e** recrystallized Xtm IIIa close to the rim of Xtm I with oscillatory zoning; **f** recrystallized Xtm IIIb with relics of Xtm I. Abbreviations after Whitney and Evans (2010); Cof - coffinite, Chrl - cheralite, Clm - clay minerals

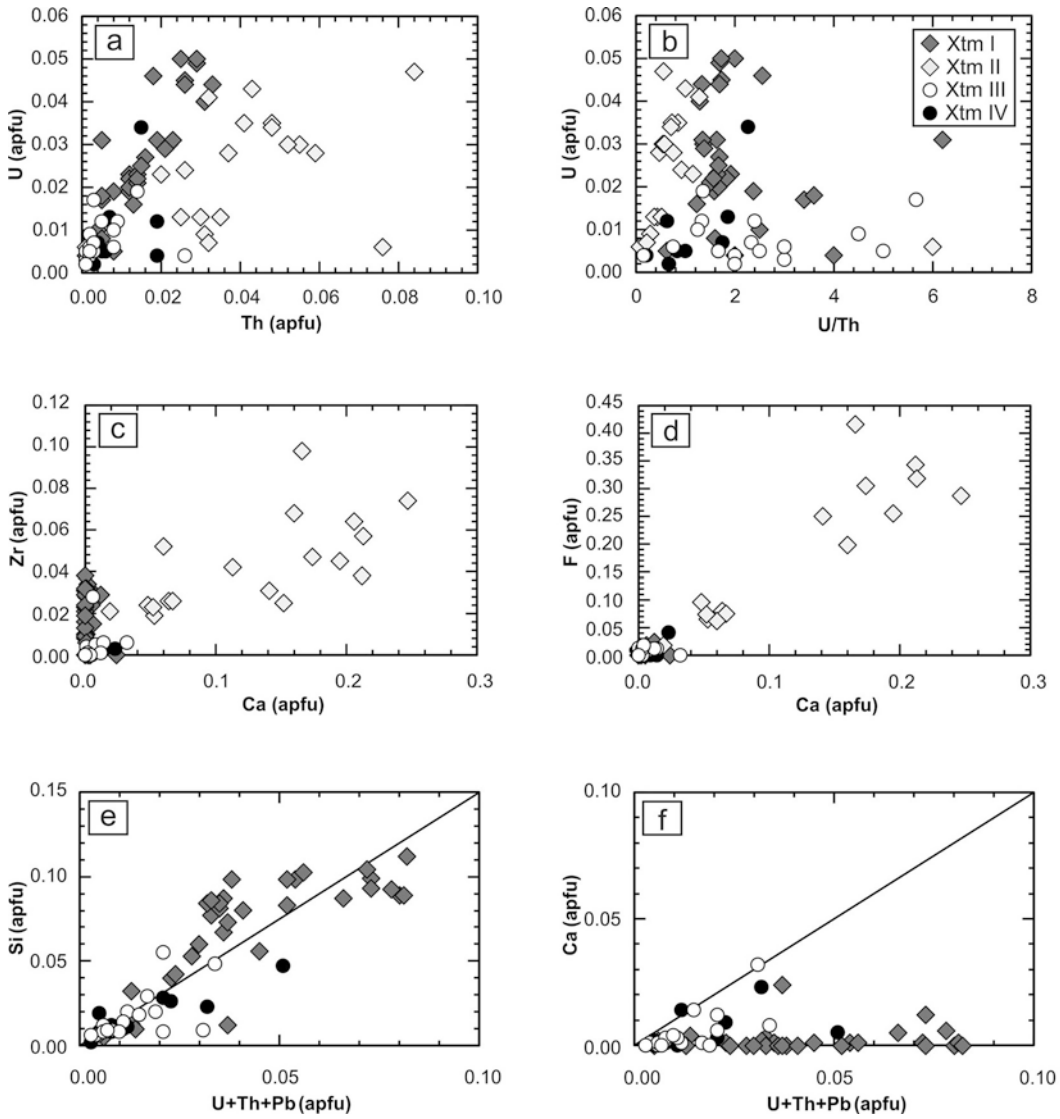

Fig. 3 Binary plots visualising the chemical composition of xenotime: **a** U vs. Th; **b** U vs. U/Th; **c** Zr vs. Ca; **d** F vs. Ca; **e** Si vs. U+Th; **f** Ca vs. U+Th

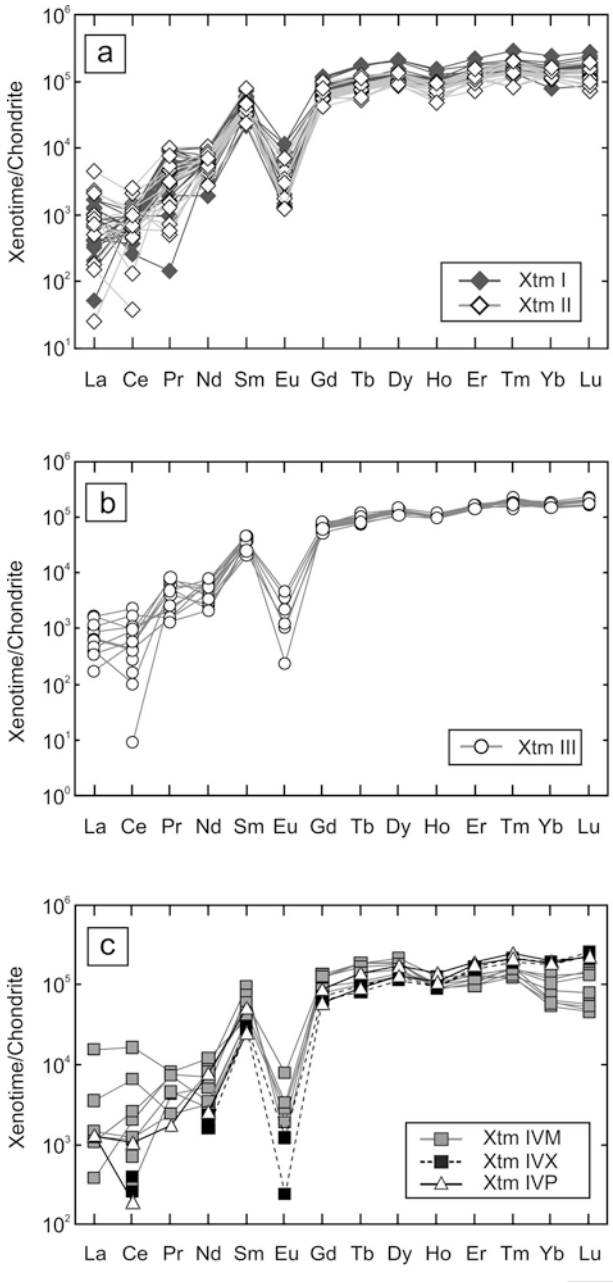

Fig. 4 Chondrite-normalized REE-patterns of xenotime (chondrite values after Taylor and McLennan 1985): **a** primary unaltered Xtm I and altered Xtm II; **b** recrystallized xenotime (III); **c** Xtm IV occurring in monazite (IVM), along fractures in primary xenotime (IVX) and as inclusions in U-rich Y,REE,Ti,Nb-oxides (IVP)

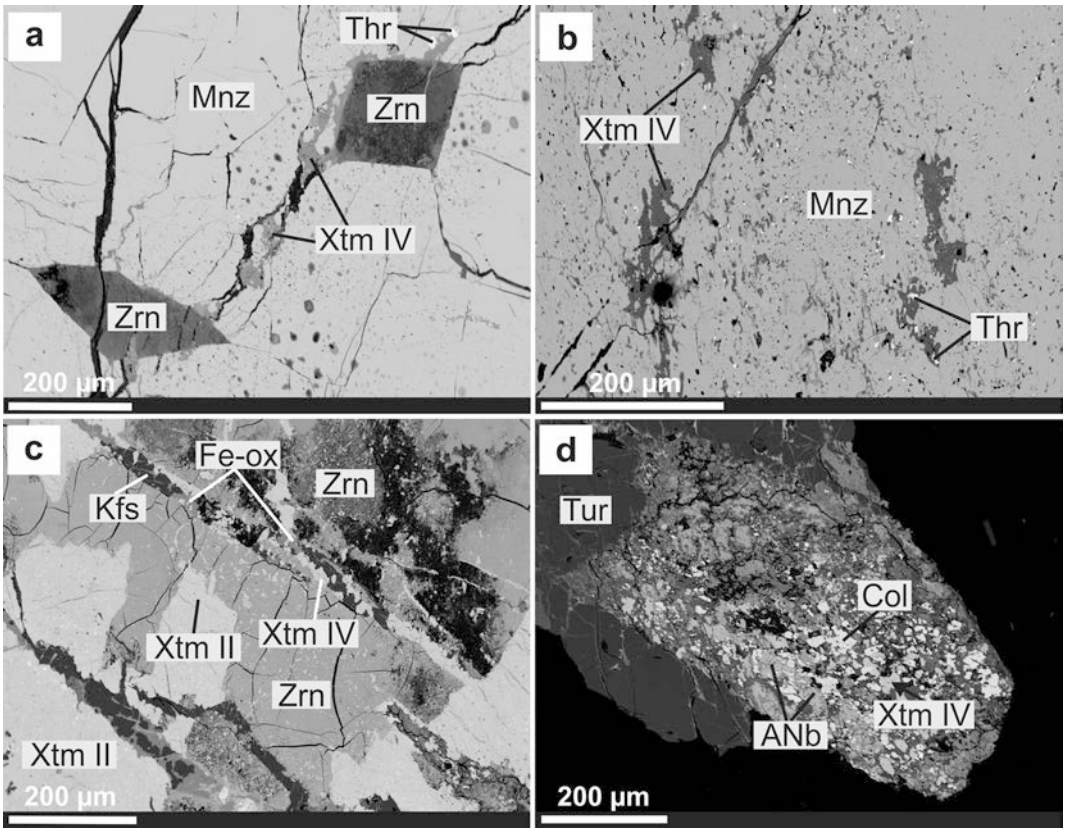

Fig. 5 BSE images of xenotime IV: **a** Xtm IV developed along fractures in monazite-(Ce) and accompanied by tiny thorite inclusions; **b** Xtm IV and thorite inclusions enclosed in monazite-(Ce); **c** Xtm IV associated with Fe-oxides, K-feldspar and limonite along fractures in altered Xtm II intergrown with zircon; **d** inclusions of xenotime and columbite after altered (Y,REE,Ti,Nb)-oxides. Abbreviations after Whitney and Evans (2010); Fe-ox = Fe-oxides; Col = columbite; ANb = amorphous hydrated Nb,Ti,U,Y,As,Si,P,Fe,Ca-phases

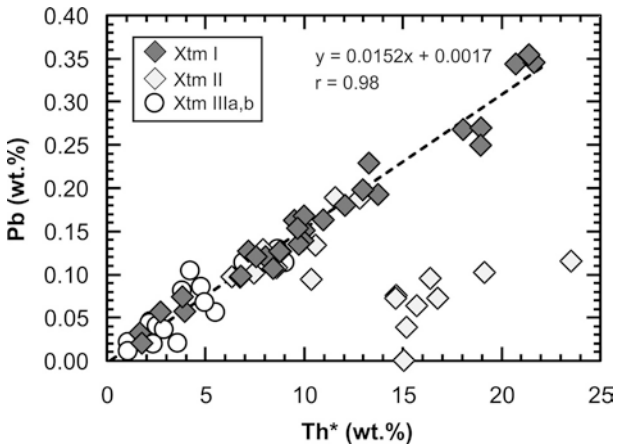

Fig. 6 Th*–Pb plot for xenotime showing isochron and regression equation for Xtm I. Th* equals to the theoretical Th content, which would produce the measured Pb for the relevant calculated age

Accepted manuscript of the published article: Miner Petrol (2016) 110:747–765 [DOI 10.1007/s00710-016-0442-6]

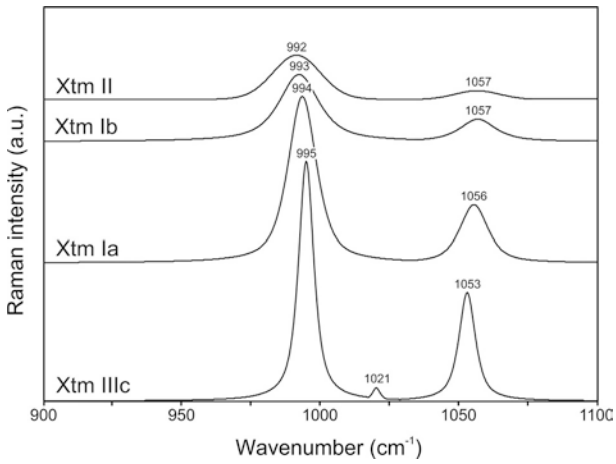

Fig. 7 Representative Raman spectra of different xenotime generations (see Fig. 2c). Original spectra were background-corrected and are shown with vertical offset for clarity

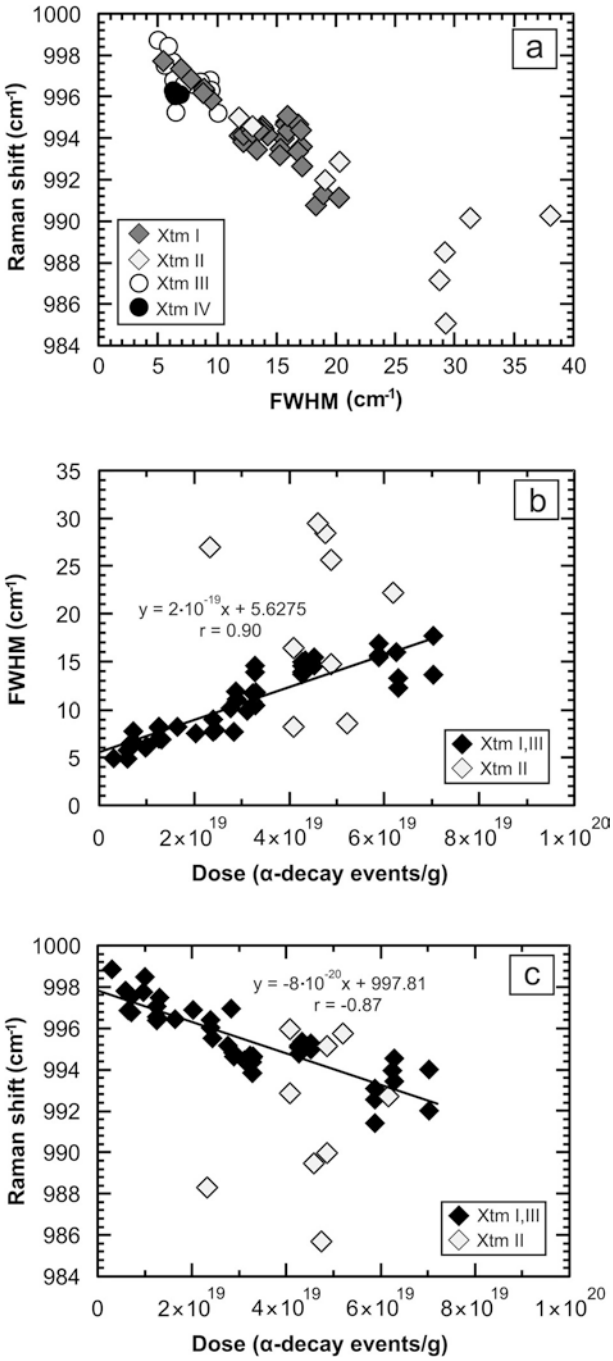

Fig. 8 Binary plots showing correlations among Raman spectral parameters and cummulkative alpha dose: **a** Raman-shift vs. FWHM of the main Raman band; **b** FWHM of the main Raman band vs. cumulative radiation dose; **c** spectral position of the main Raman band vs. cumulative radiation dose

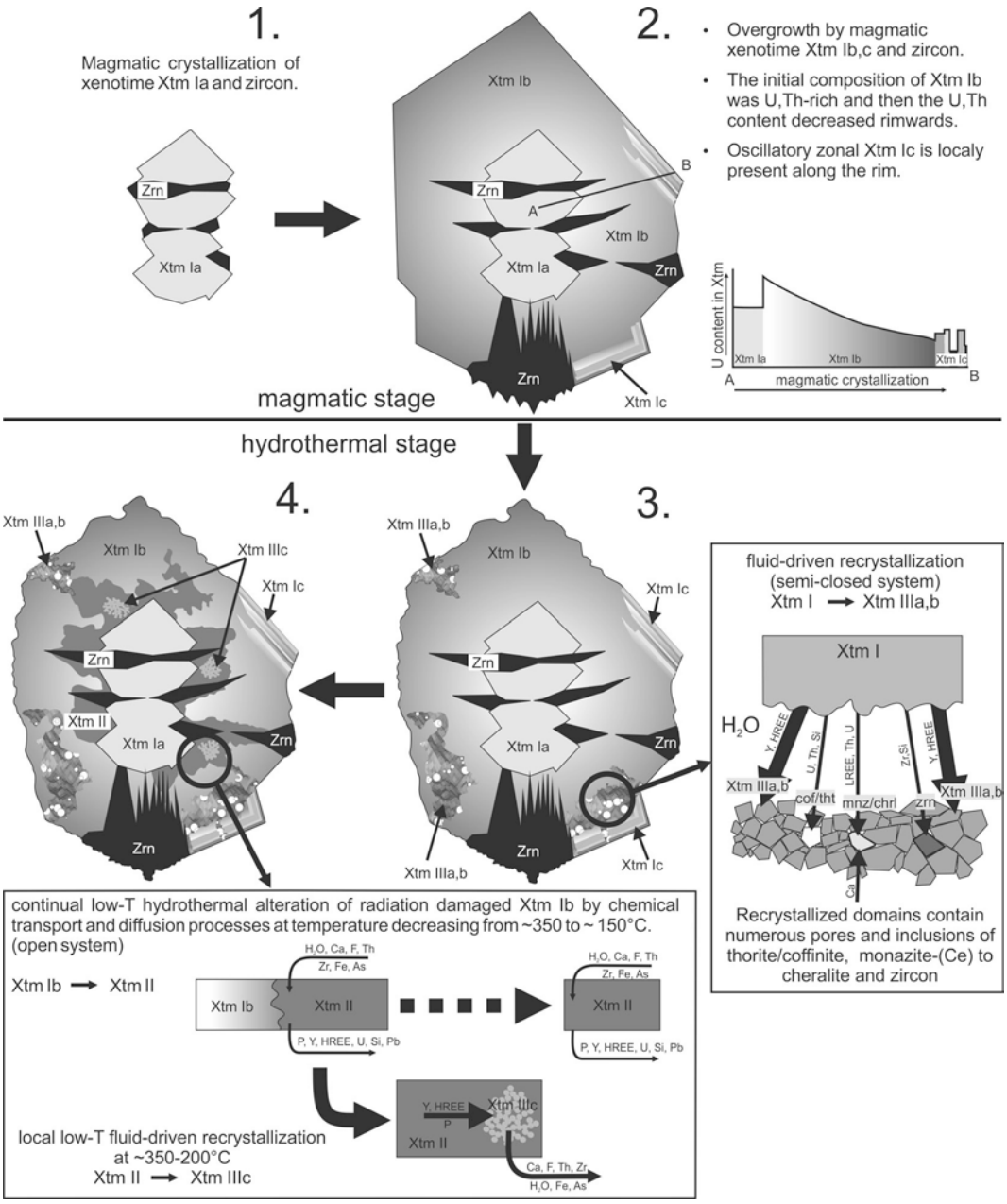

Fig. 9 Summary sketch of xenotime evolution from magmatic to hydrothermal stages

Accepted manuscript of the published article: Miner Petrol (2016) 110:747–765 [DOI 10.1007/s00710-016-0442-6]

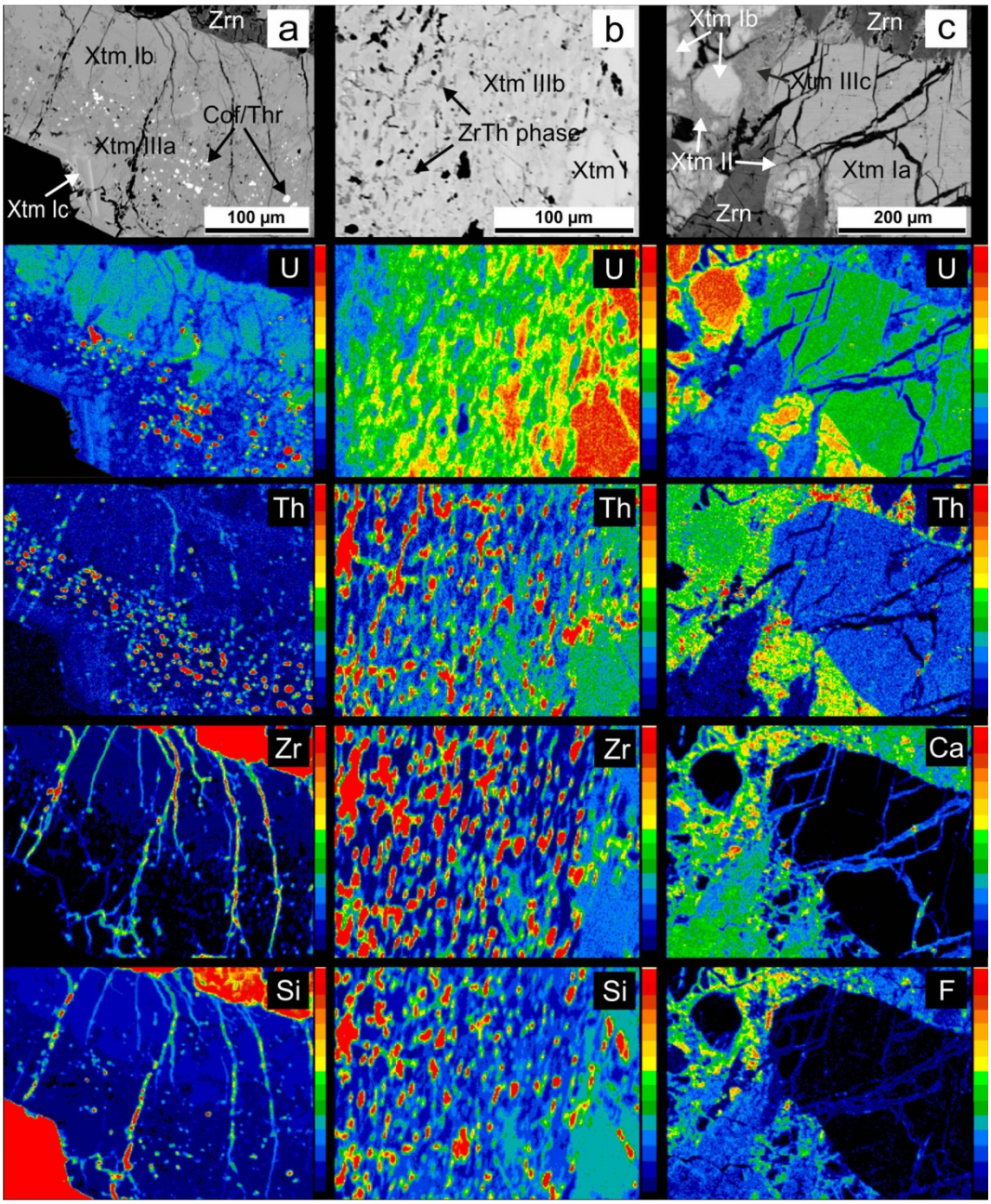

Fig. 10 X-ray element maps of xenotime: **a** primary unaltered xenotime (Xtm Ia,b) and altered domains (Xtm II) with recrystallized Xtm IIIc; **b** recrystallized Xtm IIIa containing tiny coffinite-thorite and cheralite inclusions and primary Xtm I; **c** recrystallized Xtm IIIb with Zr,Th,U-rich silicate inclusions and primary unaltered Xtm Ib

Accepted manuscript of the published article: Miner Petrol (2016) 110:747–765 [DOI 10.1007/s00710-016-0442-6]

Table 1 Results of representative EPMA analyses, calculated alpha doses, and parameters of the main A_{1g} Raman band of the xenotime

	Primary Xtm crystals and relics						Altered Xtm				Recrystallised Xtm					Secondary Xtm				det.limit *
Domain	Ia	Ia	Ib	Ib	Ic	Ic	II	II	II	II	IIIa	IIIa	IIIb	IIIb	IIIc	IV	IV	IV	IV	[μg/g]
Analysis	1	2	3	4	5	6	7	8	9	10	11	12	13	14	15	16	17	18	19	
Results of EPMA chemical analyses (all values in wt%):																				
SO_3	b.d.l.	b.d.l.	b.d.l.	b.d.l.	b.d.l.	b.d.l.	b.d.l.	0.11	b.d.l.	0.16	b.d.l.	b.d.l.	0.08	b.d.l.	b.d.l.	b.d.l.	b.d.l.	b.d.l.	b.d.l.	330
P_2O_5	32.37	31.36	30.76	30.32	34.62	34.40	33.00	31.48	26.89	24.65	34.93	35.48	33.24	34.18	36.01	34.15	35.37	35.23	34.17	380
As_2O_5	b.d.l.	b.d.l.	b.d.l.	b.d.l.	b.d.l.	b.d.l.	0.34	0.23	0.40	0.68	b.d.l.	b.d.l.	b.d.l.	b.d.l.	b.d.l.	b.d.l.	b.d.l.	b.d.l.	b.d.l.	340
SiO_2	2.54	2.87	3.01	3.22	0.21	0.97	0.87	0.86	1.25	0.78	0.19	0.28	1.42	0.85	0.32	0.83	0.57	0.24	0.07	130
UO_2	2.62	2.98	5.77	6.46	0.57	1.13	0.96	1.66	5.22	3.39	0.29	0.66	2.53	1.57	0.80	1.76	0.27	0.62	0.24	540
ThO_2	1.58	1.84	3.35	3.72	0.16	0.72	4.12	3.15	5.13	5.82	0.09	0.35	1.75	0.60	0.17	0.93	0.34	0.34	0.10	510
ZrO_2	1.86	2.27	1.71	1.71	b.d.l.	0.54	1.23	1.35	2.60	2.96	b.d.l.	0.05	0.29	b.d.l.	b.d.l.	b.d.l.	b.d.l.	b.d.l.	b.d.l.	520
La_2O_3	b.d.l.	b.d.l.	b.d.l.	b.d.l.	b.d.l.	b.d.l.	b.d.l.	b.d.l.	b.d.l.	b.d.l.	b.d.l.	b.d.l.	b.d.l.	b.d.l.	b.d.l.	b.d.l.	b.d.l.	b.d.l.	b.d.l.	780
Ce_2O_3	0.12	0.10	0.10	0.11	b.d.l.	0.09	0.07	b.d.l.	0.07	0.07	0.10	b.d.l.	0.18	0.12	b.d.l.	0.08	0.28	b.d.l.	b.d.l.	580
Pr_2O_3	b.d.l.	b.d.l.	0.11	b.d.l.	b.d.l.	b.d.l.	b.d.l.	b.d.l.	b.d.l.	b.d.l.	b.d.l.	b.d.l.	b.d.l.	b.d.l.	b.d.l.	b.d.l.	b.d.l.	b.d.l.	b.d.l.	1100
Nd_2O_3	0.47	0.45	0.47	0.44	0.14	0.53	0.60	0.51	0.38	0.37	0.43	0.49	0.56	0.58	0.53	0.67	0.26	0.17	0.19	1230
Sm_2O_3	0.91	0.90	0.86	0.84	0.79	0.99	0.88	0.91	0.76	0.71	0.95	1.06	0.79	0.81	1.03	2.13	0.82	0.68	0.57	710
Eu_2O_3	b.d.l.	b.d.l.	b.d.l.	0.08	b.d.l.	b.d.l.	b.d.l.	b.d.l.	b.d.l.	b.d.l.	b.d.l.	b.d.l.	b.d.l.	b.d.l.	b.d.l.	b.d.l.	b.d.l.	b.d.l.	b.d.l.	640
Gd_2O_3	2.12	2.08	2.01	1.99	2.29	2.29	2.09	2.09	1.77	1.58	2.25	2.38	1.89	1.93	2.40	4.08	2.70	2.14	1.77	780
Tb_2O_3	0.51	0.55	0.48	0.52	0.58	0.50	0.49	0.51	0.44	0.38	0.66	0.59	0.49	0.47	0.60	1.01	0.76	0.54	0.50	870
Dy_2O_3	4.16	4.20	4.11	3.88	5.18	4.30	4.29	3.92	3.82	3.25	4.85	4.51	4.21	4.32	4.59	6.58	5.32	4.42	4.59	860
Ho_2O_3	0.74	0.77	0.80	0.81	0.96	0.86	0.87	0.82	0.85	0.75	0.98	0.98	0.95	0.95	0.85	0.79	0.82	0.84	0.98	1600
Er_2O_3	3.26	3.35	3.01	3.15	4.14	3.19	3.08	3.03	2.80	2.40	3.84	3.28	3.70	3.76	3.45	2.41	2.69	3.83	4.10	820
Tm_2O_3	0.69	0.66	0.51	0.64	0.78	0.63	0.72	0.56	0.70	0.49	0.76	0.75	0.70	0.78	0.73	0.62	0.57	0.78	0.78	930
Yb_2O_3	3.83	3.76	3.39	3.47	4.85	3.77	3.55	3.55	2.96	2.78	4.19	3.72	4.22	4.43	4.02	1.63	2.62	4.87	4.76	870
Lu_2O_3	0.57	0.56	0.55	0.52	0.92	0.64	0.58	0.55	0.48	0.34	0.77	0.67	0.76	0.84	0.73	0.23	0.51	0.99	0.90	800
Y_2O_3	40.76	40.18	38.72	37.91	42.64	44.15	38.44	38.07	31.66	27.81	43.69	45.11	41.29	43.45	43.43	41.25	46.07	44.31	44.32	460
Sc_2O_3	0.02	b.d.l.	b.d.l.	b.d.l.	b.d.l.	b.d.l.	0.02	0.05	0.12	b.d.l.	b.d.l.	b.d.l.	b.d.l.	b.d.l.	b.d.l.	0.06	b.d.l.	b.d.l.	b.d.l.	120
Al_2O_3	b.d.l.	b.d.l.	b.d.l.	b.d.l.	b.d.l.	b.d.l.	b.d.l.	b.d.l.	b.d.l.	b.d.l.	b.d.l.	b.d.l.	b.d.l.	b.d.l.	b.d.l.	b.d.l.	b.d.l.	b.d.l.	b.d.l.	190
FeO	b.d.l.	b.d.l.	b.d.l.	b.d.l.	b.d.l.	b.d.l.	0.29	1.03	0.10	2.35	b.d.l.	b.d.l.	b.d.l.	b.d.l.	b.d.l.	b.d.l.	b.d.l.	b.d.l.	b.d.l.	120
PbO	0.11	0.16	0.26	0.36	b.d.l.	b.d.l.	0.08	0.09	0.09	0.06	b.d.l.	b.d.l.	0.11	b.d.l.	b.d.l.	0.07	b.d.l.	b.d.l.	b.d.l.	350
CaO	b.d.l.	b.d.l.	0.04	b.d.l.	b.d.l.	b.d.l.	0.52	1.38	4.41	5.07	b.d.l.	0.05	0.22	0.03	0.09	0.09	b.d.l.	0.03	b.d.l.	340
F	0.07	0.11	0.09	b.d.l.	0.09	0.10	0.16	0.67	2.62	2.56	0.12	0.12	0.09	0.11	0.12	b.d.l.	0.11	0.10	b.d.l.	460
O=F	-0.03	-0.05	-0.04	0.00	-0.04	-0.04	-0.07	-0.28	-1.10	-1.08	-0.05	-0.05	-0.04	-0.05	-0.05	0.00	-0.05	-0.04	0.00	
total	99.35	99.13	100.14	100.32	98.88	99.81	97.24	96.42	94.42	88.33	99.08	100.52	99.47	99.88	99.86	99.37	100.17	100.13	98.09	
Empirical formulae were calculated on the basis of 4 anions (in apfu = atoms per formula unit):																				
S^{5+}	0.000	0.000	0.000	0.000	0.000	0.000	0.000	0.003	0.000	0.005	0.000	0.000	0.002	0.000	0.000	0.000	0.000	0.000	0.000	
P^{5+}	0.926	0.907	0.898	0.891	0.993	0.970	0.967	0.933	0.837	0.819	0.994	0.991	0.956	0.972	1.005	0.979	0.985	0.993	0.988	
As^{5+}	0.000	0.000	0.000	0.000	0.000	0.000	0.006	0.004	0.008	0.014	0.000	0.000	0.000	0.000	0.000	0.000	0.000	0.000	0.000	
Sl^{4+}	0.086	0.098	0.104	0.112	0.007	0.032	0.030	0.030	0.046	0.031	0.006	0.009	0.048	0.029	0.011	0.028	0.019	0.008	0.002	
Sum B	1.012	1.005	1.002	1.003	1.000	1.002	1.003	0.970	0.891	0.869	1.000	1.000	1.006	1.001	1.016	1.007	1.004	1.001	0.990	

Accepted manuscript of the published article: Miner Petrol (2016) 110:747–765 [DOI 10.1007/s00710-016-0442-6]

U^{4+}	0.020	0.023	0.044	0.050	0.004	0.008	0.007	0.013	0.043	0.030	0.002	0.005	0.019	0.012	0.006	0.013	0.002	0.005	0.002
Th^{4+}	0.012	0.014	0.026	0.029	0.001	0.005	0.032	0.025	0.043	0.052	0.001	0.003	0.014	0.005	0.001	0.007	0.003	0.003	0.001
Zr^{4+}	0.031	0.038	0.029	0.029	0.000	0.009	0.021	0.023	0.047	0.057	0.000	0.001	0.005	0.000	0.000	0.000	0.000	0.000	0.000
La^{3+}	0.000	0.000	0.000	0.000	0.000	0.000	0.000	0.000	0.000	0.000	0.000	0.000	0.000	0.000	0.000	0.000	0.000	0.000	0.000
Ce^{3+}	0.001	0.001	0.001	0.001	0.000	0.001	0.001	0.000	0.001	0.001	0.001	0.000	0.002	0.001	0.000	0.001	0.003	0.000	0.000
Pr^{3+}	0.000	0.000	0.000	0.000	0.000	0.000	0.000	0.000	0.000	0.000	0.000	0.000	0.000	0.000	0.000	0.000	0.000	0.000	0.000
Nd^{3+}	0.006	0.005	0.006	0.005	0.002	0.006	0.007	0.006	0.005	0.005	0.005	0.006	0.007	0.007	0.006	0.008	0.003	0.002	0.002
Sm^{3+}	0.011	0.011	0.010	0.010	0.009	0.011	0.010	0.011	0.010	0.010	0.011	0.012	0.009	0.009	0.012	0.025	0.009	0.008	0.007
Eu^{3+}	0.000	0.000	0.000	0.001	0.000	0.000	0.000	0.000	0.000	0.000	0.000	0.000	0.000	0.000	0.000	0.000	0.000	0.000	0.000
Gd^{3+}	0.024	0.024	0.023	0.023	0.026	0.025	0.024	0.024	0.022	0.021	0.025	0.026	0.021	0.021	0.026	0.046	0.029	0.024	0.020
Tb^{3+}	0.006	0.006	0.005	0.006	0.006	0.005	0.006	0.006	0.005	0.005	0.007	0.006	0.005	0.005	0.006	0.011	0.008	0.006	0.006
Dy^{3+}	0.045	0.046	0.046	0.043	0.057	0.046	0.048	0.044	0.045	0.041	0.053	0.048	0.046	0.047	0.049	0.072	0.056	0.047	0.051
Ho^{3+}	0.008	0.008	0.009	0.009	0.010	0.009	0.010	0.009	0.010	0.009	0.010	0.010	0.010	0.010	0.009	0.009	0.009	0.009	0.011
Er^{3+}	0.035	0.036	0.033	0.034	0.044	0.033	0.033	0.033	0.032	0.030	0.041	0.034	0.039	0.040	0.036	0.026	0.028	0.040	0.044
Tm^{3+}	0.007	0.007	0.005	0.007	0.008	0.007	0.008	0.006	0.008	0.006	0.008	0.008	0.007	0.008	0.007	0.007	0.006	0.008	0.008
Yb^{3+}	0.039	0.039	0.036	0.037	0.050	0.038	0.037	0.038	0.033	0.033	0.043	0.037	0.044	0.045	0.040	0.017	0.026	0.049	0.050
Lu^{3+}	0.006	0.006	0.006	0.005	0.009	0.006	0.006	0.006	0.005	0.004	0.008	0.007	0.008	0.009	0.007	0.002	0.005	0.010	0.009
Y^{3+}	0.733	0.730	0.711	0.700	0.769	0.783	0.708	0.710	0.620	0.581	0.781	0.792	0.746	0.777	0.762	0.743	0.806	0.785	0.806
Sc^{3+}	0.001	0.000	0.000	0.000	0.000	0.000	0.001	0.002	0.004	0.000	0.000	0.000	0.000	0.000	0.000	0.002	0.000	0.000	0.000
Al^{3+}	0.000	0.000	0.000	0.000	0.000	0.000	0.000	0.000	0.000	0.000	0.000	0.000	0.000	0.000	0.000	0.000	0.000	0.000	0.000
Fe^{2+}	0.000	0.000	0.000	0.000	0.000	0.000	0.008	0.030	0.003	0.077	0.000	0.000	0.000	0.000	0.000	0.000	0.000	0.000	0.000
Pb^{2+}	0.001	0.001	0.002	0.003	0.000	0.000	0.001	0.001	0.001	0.001	0.000	0.000	0.001	0.000	0.000	0.001	0.000	0.000	0.000
Ca^{2+}	0.000	0.000	0.001	0.000	0.000	0.000	0.019	0.052	0.174	0.213	0.000	0.002	0.008	0.001	0.003	0.003	0.000	0.001	0.000
Sum A	0.986	0.995	0.993	0.992	0.995	0.992	0.987	1.039	1.111	1.176	0.996	0.997	0.991	0.997	0.970	0.993	0.993	0.997	1.017
∑ **cat.**	1.998	2.000	1.995	1.995	1.995	1.994	1.990	2.009	2.002	2.045	1.996	1.997	1.997	1.998	1.986	2.000	1.997	1.998	2.007
O^{2-}	3.993	3.988	3.990	3.993	3.990	3.989	3.982	3.926	3.695	3.682	3.987	3.987	3.990	3.988	3.987	4.000	3.989	3.989	4.000
F^{-}	0.007	0.012	0.010	0.007	0.010	0.011	0.018	0.074	0.305	0.318	0.013	0.013	0.010	0.012	0.013	0.000	0.011	0.011	0.000
U/Th	1.67	1.64	1.69	1.72	4.00	1.60	0.22	0.52	1.00	0.58	2.00	1.67	1.36	2.40	6.00	1.86	0.67	1.67	2.00
*Time-integrated alpha doses in events / gram**:*																			
Dose	$3.0x10^{19}$	$3.4x10^{19}$	$6.5x10^{19}$	$7.3x10^{19}$	$6.1x10^{18}$	$1.3x10^{19}$	$1.9x10^{19}$	$2.4x10^{19}$	$6.4x10^{19}$	$4.7x10^{19}$	$3.1x10^{18}$	$7.4x10^{18}$	$2.9x10^{19}$	$1.7x10^{19}$	$8.4x10^{18}$	$2.0x10^{19}$	$3.5x10^{18}$	$7.0x10^{18}$	$2.7x10^{18}$
Raman results (parameters of the symmetric PO_4 stretching band) in cm^{-1} :																			
Raman shift	994.6	994.4	993.2	993.3	997.7	996.9	992.0	987.1	988.5	985.1	998.7	996.6	996.3	998.4	995.2	996.3			
FWHM	13.8	13.9	15.3	16.8	5.5	7.8	19.1	28.7	29.2	29.2	5.0	8.0	9.5	5.9	6.5	6.3			

* Limits of detection for individual elements [µg/g]

** Doses were calculated from the U and Th concentrations and an age of 339 Ma

b.d.l. = below the detection limit